Interfacial Catalysis

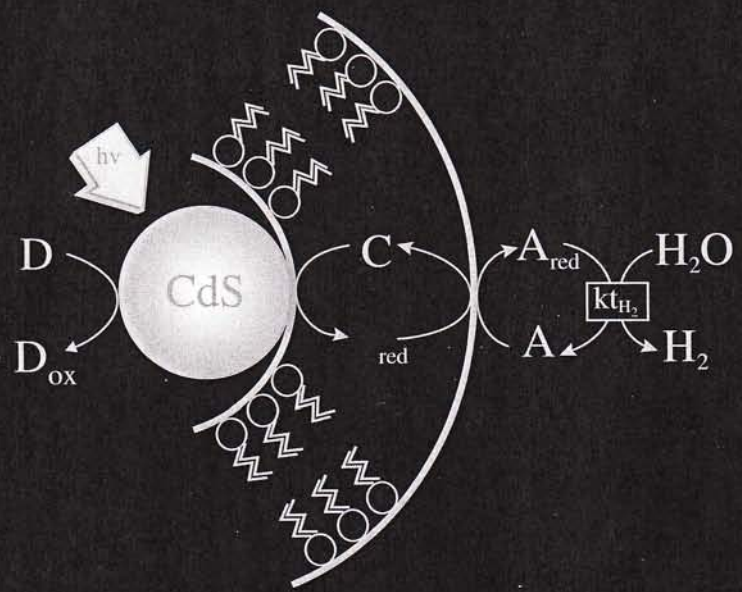

EDITED BY

Alexander G. Volkov

17

Energetics and Gating of Narrow Ionic Channels: The Influence of Channel Architecture and Lipid–Channel Interactions

PETER C. JORDAN, GENNADY V. MILOSHEVSKY, and MICHAEL B. PARTENSKII Brandeis University, Waltham, Massachusetts, U.S.A.

I. INTRODUCTION

Physiological ion channels have evolved to accomplish one basic task, using controlled ion flow to transmit electrical signals from one region of an organism to another [1]. This has many manifestations. A few examples include: sodium and potassium ion counter flows governing muscle motion (the action potential); calcium ion flow in regulating cardiac rhythms; chloride flow in regulating skeletal muscle resting potential. Structurally similar are channels that rigorously exclude ions, but transport particular neutral species (like aquaporins and glycerol facilitators) [2,3].

All such channels are designed with three aims in mind: promotion of rapid transmembrane flow of the preferred moiety (permeability); strong discrimination against the flow of any other major physiological solute (selectivity); and rigorous control of these functions (gating) so that the organism does not fall prey to dehydration or severe electrolyte imbalances.

A channel, in its conducting (open) state, behaves like (and can be described as) an enzyme, with substrate turnover typically in the range 10^6–10^7 s^{-1} and a recovery time in the range of milliseconds. Unlike pumps, where turnover is in the range 10^2–10^3 s^{-1} [4], movement through a channel is diffusive in nature and requires no addition of energy. Channels are extraordinarily effective catalysts for the transport of their chosen ion or molecule. Some quantitative estimates of their amazing success in such endeavors are readily obtained. The energy required to transfer an ion the size of K^+ across a membrane would be in excess of 200 kJ mol^{-1}. The corresponding transit time would be $\sim 10^{22}$ s or $\sim 10^{14}$ years. Quite clearly, ion channels completely suppress the electrical image barrier posed by the membrane. However, they are functionally far more impressive than this simple estimate suggests. There is strong evidence that a typical potassium channel has a narrow constriction $\sim$1.5 Å in radius and $\sim$15 Å long [5]. Treating the water-filled pore as a conducting "wire" of radius R and length L, and assuming that the ionic mobility through this pathway is determined by the aqueous equivalent conductance, λ, estimates of the pore's conductance can be given. Presuming a point ion and no wall friction, the conductance, γ, is

$$\gamma = \pi R^2 \lambda / L \tag{1}$$

for physiological concentrations of 100 mM this would imply a conductance of ~50 pS, only slightly less than that of large-conductance potassium channels, ~200 pS [1]. However, if small pore friction and access limitations are taken into consideration [6,7], the maximal γ estimate drops precipitously, to ~0.05 pS, far less than that which nature has been able to design. Not only do ion channels negate the electrostatic barrier, they do so in ways that, in effect, imply that their interiors are frictionless and their entrances are nonreflecting.

Section II discusses the energetic determinants of catalysis: permeation and selectivity. In narrow pores they are observed to have some puzzling and superficially contradictory properties. The two best studied systems are the gramicidin-A (GA) dimer and the KcsA potassium channel. Here, we limit consideration to the more physiologically important KcsA system. Our focus is on the interplay of various interactions governing ion entry into this channel, and the ion's subsequent passage through the pore. The general theoretical problem has been reviewed recently [8]. Our discussion first provides a brief overview of standard theoretical approaches to the problem, from both the microscopic and mesoscopic perspectives. We then outline the semimicroscopic Monte Carlo formalism that we have developed [9–11], highlighting its differences from the more orthodox methods and emphasizing its particular advantages. We finally apply this method to KcsA, and focus on some of the insights that it yields.

Section III describes the mechanical influence that a membrane can have on channel stabilization, focusing on simple physical models used to understand the mechanism of membrane–peptide interaction. We describe the elastic interaction between a membrane and an inserted peptide, focusing on GA, and first provide a brief overview of the basics of the elastic theory of membranes, demonstrating the formal equivalence of these issues to a classical problem in mechanical engineering. We then consider different descriptions of the interaction of a membrane with an inclusion and follow with a discussion of lipids' influences on channel lifetimes. Finally, we describe a new perspective for describing the membrane-inclusion interaction. It emphasizes the inclusion-induced perturbation of membrane elastic constants at the lipid–peptide interface.

In Section IV we extend the ideas of Section III and treat membrane-mediated interaction between peptides. First, we consider the interaction between two insertions and study the dependence of the free energy on both the interinsertion distance d, and the "contact slope" s, the normal component of the gradient of the membrane's deformational profile at the lipid–peptide interface. When minimized as a function of s this free energy, $F_{\min}(d)$ is repulsive for all d. However, when treated for fixed s, the profiles $F_s(d)$ undergo a van der Waals-like transition from attractive behavior for $s \geq s_{cr}^{(1)}$ to repulsive behavior for $s \leq s_{cr}^{(2)}$; in the intermediate region, the profiles exhibit a local minimum separated by a barrier from a repulsive region at larger d. Finally, we focus on multiparticle effects, particularly those involving five and seven insertions and find that many-body interactions smooth out the repulsive behavior of $F_{\min}(d)$ for a cluster of five and make it purely attractive for a cluster of seven. Treated at fixed s, the profiles $F_s(d)$ are similar to those found for two insertions, with three distinct regions and two "critical" points.

Section V summarizes our results and outlines promising avenues for future work. Of particular interest are how increasing the insertion concentration may lead to phase transitions and may affect the lifetime of ion channels.

II. SELECTIVITY AND PERMEABILITY: CATALYSIS IN NARROW PORES

Selectivity and permeability are essentially the mappings of differential free energy profiles for the various transportable species. As such they are sensitive to the membrane, which

provides low dielectric surroundings for the channel protein. The energetic determinant of permeation is that the favored species' permeation free energy profile is essentially flat; relative to the free energy of the aqueous ion there should be neither a deep well (leading to block) nor a high barrier (leading to impermeability). All competing species must have significantly higher barriers to permeation in some region of the permeation pathway and must not have any deeper wells where they might effectively block the channel. This can require a highly sophisticated discrimination mechanism. Potassium channels rigorously exclude sodium; clearly, this is not just molecular sieving. When no calcium is present, calcium channels are highly permeable to sodium; however, at physiological calcium concentrations (a few millimolar) the predominant sodium (150 mM) can no longer pass. Aquaporins and glycerol channels permit neutral molecules to pass; much smaller ions do not enter the channel.

A. Free Energy Compensation and Molecular Structure

Both permeability and selectivity are determined by a moiety's "permeation free energy profile," the difference between its solvation free energy within the channel ($\Delta G_{\text{solvation}}$) and its free energy in bulk water ($\Delta G_{\text{hydration}}$). Discrimination between solutes in the channel interior requires a relatively narrow pore; otherwise the most that can be expected is sieving in response to ionic polarity. In traversing the pore there are major changes in the solute's local solvation environment. Physiologically significant ions are fully hydrated in water, with approximately six to eight surrounding solvent molecules in their first hydration shell [12]. As an ion enters the pore most of this water is stripped away, and depending on the radius of the channel constriction, it may be left with only a pair of water molecules, one leading and one trailing. The remainder of its immediate solvation environment is composed of functional groups from the channel peptide. Rapid turnover requires that this environment be essentially as "solute friendly" as bulk water. How might ions be stabilized within channels? Given the structure of the amino acid building blocks, there are some obvious candidates: cations could interact favorably with backbone carbonyl oxygens, with negatively charged residues or, via a polarization mechanism, with the π-electrons of aryl residues [13]; anions might couple with backbone amido hydrogens or with positively charged residues. How might charged groups be excluded from transmembrane aqueous pathways? Possibly this might involve electrostatic rejection by apolar channel surroundings. In the absence of structural clues, choosing among these alternatives is purely speculative.

Detailed structural data are only available for a few highly selective channels. The best characterized is the model system gramicidin, which has been elucidated using NMR-based techniques [14,15]. Among physiological systems, atomic level resolution structures (based on x-ray or cryoelectron microscopy) are available for a potassium channel from *S. lividans* (KcsA) [5], two prokargotic chloride channels [16], a stretch activated channel from *M. tuberculosis* [17], human red cell aquaporin-1 [18], and a glycerol facilitator from *E. coli* [19]. All share a common feature, a narrow region where the transported species must shed most of its surrounding water and become intimately associated with the channel protein. In KcsA the constriction is associated with a single file region structurally much like that in gramicidin, but far shorter, only ~10–15 Å long; there are backbone carbonyl oxygens with which the ions could co-ordinate. The chloride channel's structure [16] confirms the "double-barreled shotgun model" [25]; anion stabilization arises by interaction with a number of partially positively charged groups. In both aquaporin-1 and

the glycerol facilitator, the nonpolar groups that line the long single file would appear to form inhospitable surroundings for ionic species.

Atomic level resolution structures are not yet available for sodium or calcium channels or for nicotinic receptors. Electrophysiological inference suggests strongly that the selectivity domain of calcium channels involves four glutamates; in the sequentially similar sodium channels three of these have been replaced by an alanine, and aspartate and a lysine, mutating a region with net charge of -4 to one with net charge of -1 [20,21]. There are structural data on the acetylcholine receptor (AChR, the most heavily studied member of the nicotinic receptor family), but at just below the resolution required for detailed theoretical analysis [22]; nonetheless, electrophysiology suggests that, in AChR itself, sets of negatively charged residues create annular regions of negative potential in the channel, and that these regions stabilize cations and exclude anions [23]. As yet there is no clear structural basis for the mild univalent/divalent discrimination observed [24].

Gramicidin's structural stability arises from hydrogen bonds between backbone carbonyl oxygens and backbone amido hydrogens. Cation entry locally disrupts the hydrogen bonds with simultaneous local co-ordination to two or more oxygens. As the ion becomes solvated by the groups forming the channel backbone, all but two of its waters of solvation must be stripped off. Whether the origin of the channel's cation selectivity is primarily due to the channel carbonyl's ability to co-ordinate positive ions [26] or reflects, in roughly equal measure, the greater difficulty of partially dehydrating anions [9] is still open to dispute.

The KcsA structure exhibits numerous features consistent with electrophysiological inferences [5]. As had been deduced, the channel is effectively a cylindrically symmetrical tetramer. In further accord with biochemical evidence, there are negatively charged residues near the channel mouths, augmenting and depleting the concentrations of cations and anions, respectively. Kinetic models of the permeation pathway implied a multi-ion channel [27]; this was corroborated by the x-ray structure, which displays three ions in the pore. The local filter architecture, a narrow constriction lined with carbonyl oxygens, provides clear rationalization for this multi-ion stability. As illustrated in the idealization of Fig. 1, two ions, separated by a single water molecule, are each surrounded by eight carbonyl oxygens; the third is in a small aqueous pool with the carboxyl termini of the four α-helices aimed directly towards its center. However, the ionic pathway in this filter is so narrow (with a mean constriction radius $\sim$1.4 Å) [28] that it is not obvious how an ion can pass through it essentially unimpeded. In fact, recent electrophysiological evidence suggests that the selectivity filter in KcsA may have undergone a conformational change in the transition to the open state of the channel, since ions as large as tetramethylammonium (TMA, radius $\sim$2.9 Å) appear to permeate effectively [29]. Even in this well-characterized system, unresolved questions remain. How can the free energy profile for potassium be essentially barrierless; i.e., why is potassium conductance so high? If the conducting channel is $\sim$5.8 Å in diameter, what makes sodium permeation effectively impossible?; i.e., why is the K/Na permeability ratio so high? How does the structure translate into a free energy profile that accounts for the macroscopic observations?

B. Modeling Conductance and Permeation Free Energy

The basic goal in theoretical modeling of ion channels is relating molecular structure to physiological function (for a recent comprehensive review, see Ref. 8). A wide range of approaches have been used in this quest, most often targeted at the valence-selective simple model channel, gramicidin [e.g., 9,30–34]. Here, our focus is a truly ion-selective

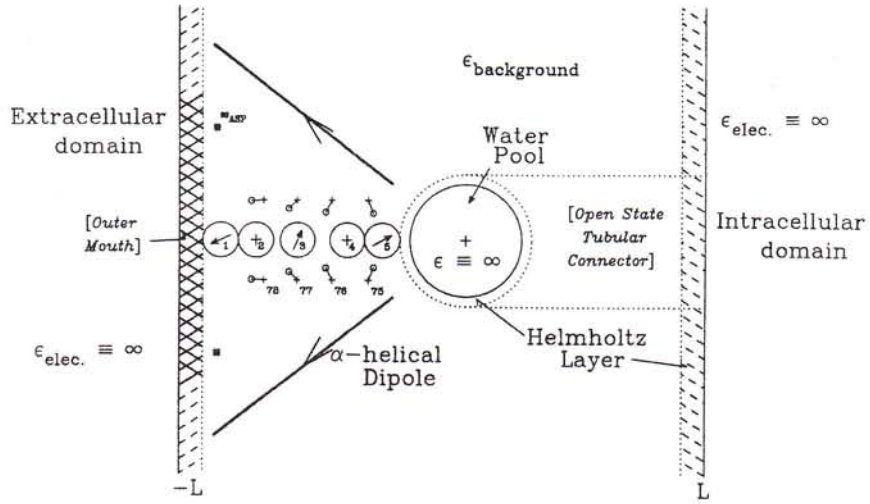

FIG. 1 Semimicroscopic model geometry for the KcsA selectivity filter. It includes solvating CO groups (residues 75–78 of each tetramer strand), single file ions and waters, peptide dipoles, the ^{80}Asp carboxylates, and the aqueous cavity and its included ion. In its simplest form, bulk electrolyte and the cavity are treated as dielectric continua. The Helmholtz layer (accounting for water immobilized by interaction with polar surfaces) separating the explicit sources in the filter from extracellular bulk water has a width of 2 Å; that between the filter and the midchannel water pool is 1.5 Å. As illustrated, the pool radius is 5.0 Å. The crystallographic occupancy sites (2 and 4) are ~ 18.5 and 11.0 Å from the center of the water pool. In modifications including more explicit water, the pool accommodates ~20 waters. Two optional geometry modifications involving additional explicit waters are indicated in italics. For modeling an open channel the pool is deformed into a tubular connector (dotted lines). To describe better the influence of the outer mouth on ion-filter energetics, the heavily cross-hashed region in the left Helmholtz layer can be filled with explicit water.

physiological system, the well-characterized KcsA potassium channel, which has recently become the object of much scrutiny, using both microscopic and mesoscopic methods.

1. Conventional Approaches

Both molecular dynamics (MD) simulation and Monte Carlo (MC) computation of equilibrium behavior can be carried out at full atomic detail, but each makes large computational demands. Were atomic motions adequately represented by Newtonian mechanics (reasonable unless some mechanistic steps depended heavily on proton transfers [33]), either could, in principle (with runs sufficiently long), provide an accurate, well-resolved and reliable picture of ionic energetics along a permeation pathway (for reviews focusing on biophysical applications, see Refs 32,35,36). There are, however, well-known difficulties with these approaches. The results are only as reliable as the underlying force field, which must correctly describe interactions among the atoms of both the protein and its surrounding solvents (cell membrane, external water, and cytoplasmic water). Since the ion–atom terms in the typical force field have been parameterized to mimick behavior in

aqueous solutions, it is uncertain if they adequately account for ion–solvent interaction in the channel interior, where both water and ion–water structures differ sharply from that in bulk solution. Certainly, the effective water–water potentials used in most MD and MC studies bear no resemblance to quantum mechanically determined water dimer potentials [37]; this strongly suggests that either polarization or explicit three-body interactions [38] must be included if water is to be accurately modeled under conditions sharply different from those used in the parameterization (ambient water). As these microscopic approaches are computationally very time consuming, individual simulations are rarely if ever repeated using fundamentally different force fields. Thus, their reliability can only be established by whether the computational setup is satisfactory and whether the results are, by and large "reasonable," i.e., in agreement with experimental observation and physical preconception. If this is the case, then credence is given to unusual observations.

Recent applications of MD simulational have addressed a wide range of issues. Clear evidence has been adduced to show that the permeant ions play a significant role in stabilizing the channel assembly [39]. A detailed model of the channel's duty cycle, involving concerted movements of a K^+–H_2O–K^+ cluster from the aqueous cavity through the filter [40], was found to be an energetically favorable permeation pathway. Somewhat unexpectedly, a computation of the multi-ion free energy profile suggests that the channel might possibly operate in a four-ion mode, with one ion in the cavity and three additional ions in the filter, each separated by a single water molecule [41]. There is evidence that the oriented α-helices, in addition to helping to stabilize the ion in the cavity, align the water molecules of the cavity and thereby contribute indirectly to stabilizing the ions in the filter [42]. While ionic diffusion appears to be significantly slowed in the channel, permeation is not hindered since it appears driven by coulombic repulsion between the ions in the filter [28,43]. In all cases where computations have addressed the issue of selectivity the results accord qualitatively with the observed high K/Na permeability ratio. However, the structural basis for this discrimination remains an open question. Possibly it reflects the rigidity of the filter, so that sodium cannot bind as effectively as potassium to the carbonyl oxygens in the binding pockets [5,11,28,40,43]. Alternatively, it may be a reflection of the greater energetic cost of dehydrating Na, i.e., removing it from water [44]. Most of these simulational results are consistent with experimental observations on the conducting channel. A few are surprising and none is contradictory. Their internal consistency provides a strong indication that, by and large, they realistically describe significant aspects of the interaction between ions and the KcsA selectivity filter. However, given that the x-ray structure describes a constriction that is just large enough to accommodate Cs^+ [5], the largest of the alkali cations, what is uncertain is whether any of these MD results is truly descriptive of behavior in the open state of KcsA, which appears to be permeable to the much larger TMA [29].

Mesoscopic studies begin by drastically simplifying the computational model or, in cases where direct structural data are unavailable, building models based on electrophysiological inference [45–48]. Instead of treating a fully hydrated KcsA channel embedded in a model membrane or surrounded by a domain formed from aliphatic chains [28,39–44], the solvents (exterior water, cytoplasmic water, and the membrane) are replaced by dielectric continua [49,50]. The fraction of the peptide that is explicitly included in the model system depends on the specific aspects of channel behavior that are under investigation. In computations designed to model conductance, the model's geometry necessarily differs from that determined crystallographically, where the channel, at its intercellular end, is far too narrow to permit ion entry. In all mesoscopic modeling only a very few moieties are assigned mobility. The goal is not detailed simulation of behavior at the atomic level, but

development of a (more or less realistic) model that accords with a specified range of the channel's properties. The results of such modeling are crucially dependent on the simplifying assumptions employed. Their ultimate goals must be limited; there will always remain some ambiguity in the correlations of molecular structure with physiological function. However, whenever the results of dissimilar theoretical approaches, based on rather different (but plausible) physical assumptions, are in basic agreement, their overlap provides strong evidence for the fundamental correctness of a particular correlation.

In a study of the electrostatic influence of the oriented α-helices and the aqueous cavity in stabilizing an ion in the cavity [49], stringent dielectric assumptions were imposed. All aqueous regions were treated as dielectrically equivalent to bulk water, with an ε of ~80, an approximation that must break down in the narrow constriction, where the effective ε is more likely to be in the range ~2–4 (this choice was first suggested and discussed in Refs 51 and 52) [53,54]. The solvating protein was treated as an immobile set of charges at their crystallographic locations and embedded in a continuum dielectric with $\varepsilon = 2$; this approximation ignores the stabilizing influence of solute-induced solvent reorganization, which would tend to raise the effective ε. These constraints have important consequences: the first overestimates dielectric shielding in the constriction, leading to much reduced interionic repulsion; the second ignores electrically induced reorientation of the peptide's charged and polar groups, sharply increasing the strength of the electrical interaction (both attractive and repulsive) between the peptide and ions in the channel. Nonetheless, the conclusions are illuminating and clearly demonstrate a direct relation between the channel's structure and its kinetic properties. Consistent with the x-ray structure and the properties of K-channels generally, monovalent cations were found to be more stable in the cavity than in bulk water. Further consistence with the general behavior in K-channels, divalent cations were also more stable in the cavity than in bulk water, but significantly less stable than the monovalent cations.

A completely different mesoscopic study used crystallographic data as input for Brownian dynamics analysis, with the aim of modeling potassium channel conductance using the KcsA structure as a guide [50]. The only parts of the KcsA assembly specifically incorporated were the charged residues near the channel mouths, the carbonyl oxygens lining the constriction, and the carboxyl termini of the helix dipoles; the positions of all these moieties were fixed, and determined from the x-ray structure. Dielectric conditions similar to those of the electrostatic [49] analysis were imposed ($\varepsilon = 2$ in nonaqueous regions and a constant, but adjustable, ε extending the length of the aqueous pore). An extracrystallographic assumption, based on electrophysiological observations, fixed the channel diameter of the intracellular mouth at ~6.0 Å, consistent with studies of the interior block. The diameter of the channel constriction was fixed by the x-ray structure, and taken to be 3.0 Å. With this model, the multi-ion kinetics observed experimentally could be reproduced. Rectifying current–voltage relationships in good quantitative agreement with experiment were found when the pore was assigned an ε of 60. As with the electrostatic study [49], this too demonstrates that macroscopic observables can be directly deduced from knowledge of the channel's structure, augmented by physical assumptions based on electrophysiological inference.

2. Semimicroscopic Method

While they provide considerable insight into aspects of ion-channel behavior, and the relation between structure and function, the approaches outlined in Section II.B.1 have their drawbacks. The reliability of the force fields, the real time length of the simulations,

and possible complications in treating long-range interactions limit the range of applicability of microscopic studies. Also, the introduction of unconfirmable, and somewhat counterintuitive, dielectric assumptions, the use of a continuum description of water in a highly constricted environment, and the immobility of the channel's electrical surroundings limit the range of applicability of mesoscopic studies. A model treatment that bridges the gap between these methods might provide insights not readily obtained using either.

The semimicroscopic (SMC) formulation was designed for just this purpose [9]. Its basic philosophy is that a certain, limited number, of interactions are crucial determinants of ion-channel permeation that must be accounted for microscopically. These would include the contents (ions and water) of the narrow part of the channel and the solvating groups forming the boundaries of this constriction. The more distant parts of the system need only be described approximately. In the case of KcsA, these could include the protein's charged residues and the termini of the oriented α-helices. Bulk water domains, the remainder of the protein and its surrounding membrane are described as dielectric continua. Figure 1, an abstraction of the KcsA selectivity filter, illustrates how these ideas may be translated into practice. In its minimalist application, the only explicitly mobile features are the single-file moieties: ion(s), single-file waters, and the backbone carbonyl oxygens of residues 75–78 that form the lining of the selectivity filter constriction. Additional electrical features (the backbone carbonyl carbons of residues 75–78, the separated termini of the oriented α-helices, and charged amino acid residues) are immobilized. The aqueous cavity and both bulk water regions are assigned a high $\varepsilon \sim \infty$; the regions between the aqueous phases, comprising the membrane and the remainder of the peptide, are assigned a low $\varepsilon \sim 2$ [10,11]. In this way, a protein system comprising some 600 residues with another 100 or so water molecules in the extracellular mouth, the constriction, and the aqueous cavity has been described in terms of ~20 mobile units, with the remainder forming part of an electrical environment.

Unlike strictly mesoscopic approaches, the SMC method permits the inclusion of substantially more mobile molecular detail, treating various structural features both individually and collectively. Unlike the microscopic approaches, the computations are rapid enough that a wide range of plausible perturbations of the basic structure can be essayed. Both qualitative and quantitative consequences of significant structural changes can be readily determined. While the x-ray structure of KcsA depicts a very narrow filter [5], the electrophysiology suggests a substantially wider filter when the channel is in its conducting state [29]. Using the SMC protocol it is possible to carry out a range of thought experiments. A particularly interesting example would be to enlarge the filter gradually and determine how the filter radius affects channel selectivity.

This approach involves some major approximations, the most important being the dielectric constant used to describe the intramembrane region and the resulting force fields devised to describe interactions between the groups explicitly modeled. Because $\varepsilon_{\text{background}}$ is 2, standard force fields such as CHARMM [55], AMBER [56], and GROMOS [57] for which $\varepsilon_{\text{background}} \equiv 1$ are not appropriate. What is the rationale for assigning an ε of 2? The basic idea is to account for electrically induced solvent reorientation of the ion's surroundings in the channel–membrane–water ensemble, i.e., to treat the structural aspects of dielectric reorganization. Dielectric response is frequency dependent. Consider water. At low frequency ($\nu < 1$ GHz), molecular motion is effectively instantaneous; the solvent responds rapidly and in phase with an electrical stimulus. The dielectric constant does not differ from its static value [58]. At higher frequency (from ~ 1 GHz to ~ 1 THz), rotational and vibrational responses are gradually frozen out and water's dielectric constant drops from ~ 80 to its high-frequency value of 1.8, representing the electronic con-

tribution to water's dielectric permittivity. The SMC method is designed to take full account of electrically induced structural rearrangement, which suggests assigning the system a background $\varepsilon \sim 1.8$. The actual choice of $\varepsilon_{\text{background}}$ is not quite so straightforward since the ensemble also includes lipid for which the high-frequency dielectric constant is somewhat larger, ~2 [59].

One approach to a "best" value for ε is through the development of appropriate force field parameters. For the simplest SMC modeling, based on hard-core molecules and ions [9–11], this requires establishing the effective radii for water and the solute ions. Using as criteria the density of bulk water and the hydration free energies of monovalent alkali cations and halides, the optimal choice of ε is 2 with a water radius of 1.4 Å [60]. With these parameters the hydration free energies of both alkali cations and halides can be reasonably well reproduced using the Pauling radii [61]. Again, it should be stressed that SMC modeling is basically designed to establish the qualitative influence that different structural features have on permeation, and how permeation responds to structural change. High-accuracy quantitative agreement with experiment, while it would be a desirable outcome, is not an overarching goal.

C. SMC Computation of Permeation Free Energy

In ion permeation through a transmembrane channel, the basic process is one in which a fully hydrated ion is removed from water and exchanged for a water molecule in the filter. This is summarized by the reaction:

$$\text{Ion}_{\text{aqueous}} + \text{Water}_{\text{channel}} \rightarrow \text{Ion}_{\text{channel}} + \text{Water}_{\text{aqueous}} \tag{2}$$

In applications of the SMC approach the permeation process is decomposed into three distinct transfer steps. First, an ion in bulk water is *dehydrated* and exchanged for a water molecule in the gas phase; this is followed by transfer of the ion to a *cavity* in an infinite background dielectric, exchanging it for a water in the cavity; finally, the ion in the infinite dielectric background is *stabilized* by exchange for water in the channel. The individual steps are

$$\text{Ion}_{\text{aqueous}} + \text{Water}_{\text{vacuum}} \rightarrow \text{Ion}_{\text{vacuum}} + \text{Water}_{\text{aqueous}} : \textit{dehydration} \tag{3}$$

$$\text{Ion}_{\text{vacuum}} + \text{Water}_{\text{background}} \rightarrow \text{Ion}_{\text{background}} + \text{Water}_{\text{vacuum}} : \textit{cavity} \tag{4}$$

$$\text{Ion}_{\text{background}} + \text{Water}_{\text{channel}} \rightarrow \text{Ion}_{\text{channel}} + \text{Water}_{\text{background}} : \textit{stabilization} \tag{5}$$

The hydration energy is experimentally accessible (to within ± 3–4 kT at 300 K); the cavity term is a Born energy, determined by the ion's cavity radius in the channel; and the stabilization energy is computed using standard perturbation methods [9].

It should be noted that the process of Eq. (3) is actually hypothetical; nevertheless, these energies can be estimated with some considerable certainty. What is needed is the equivalent of a measurement of the absolute reduction potential for the standard hydrogen electrode (SHE), i.e., the process:

$$\text{H}^+(\text{aqueous}) + \text{e}_o^- \rightarrow \frac{1}{2}\text{H}_2(\text{gas}) \tag{6}$$

Standard tabulations of ionic free energies assign this process a reference free energy of 0.00 kJ mol^{-1}. All ionic reduction potentials are based on this standard; to compute absolute values from standard values requires shifting them by Z times the real reduction

free energy for the SHE, with Z being the ionic valence. The SHE potential cannot be directly measured. All estimates rely on reasonable, but ultimately unverifiable, assumptions [62]. The most recent experimental and theoretical determinations differ by only ~7 kT [63,64], suggesting an estimated experimental uncertainty in $\Delta G_{\text{dehydration}}$ of ~3–4 kT.

The cavity step, Eq. (4), involves the transfer of the ion from vacuum, with its ε of 1, to the dielectric background, where $\varepsilon \sim 2$, and the complementary process of transferring water from the background to vacuum. This is equivalent to two Born charging processes, one for a point charge and the other for the water charge distribution; as long as the cavities are chosen to be spherical the associated energies are readily computed [65]. Naturally, transfer energetics is dominated by the ion, but the water contribution cannot be ignored. Using a water model of radius 1.4 Å incorporating three charges located at the atomic sites that reproduce water's intrinsic dipole moment, the free energy for transfer of water is ~10 kT; for a monovalent ion of the same radius the transfer free energy is 10 times larger, i.e., ~100 kT.

The free energy defined by Eq. (4) requires establishing a "cavity radius" for the particular solvation environment. This is done by noting that, in a Born model, the ionic charge (or the water charge distribution) is in a cavity with dielectric constant of unity, surrounded by solvent domains with their associated dielectric constants. The cavity boundary is, therefore, the position where the solvent begins [66]. When viewed from a quantum mechanical perspective, this is where the ion's (or water's) charge distribution begins to overlap significantly with the charge distribution of the molecules forming the central species' first solvation shell; this is essentially the van der Waals radius of the solvent molecules. In studying ion–water systems containing a fully charged solvated ion, with the ion at the center of a first solvation sphere, the mean ion–water distance naturally exceeds the sum of the two moieties' hard-core radii [60]. Using the quantum mechanical identification, the cavity radius is simply the difference between the mean ion–water distance for molecules in this first solvation shell and water's hard-core radius; it is larger than the ion's hard-core radius [60].

The stabilization contribution, Eq. (5), in which a charge in the dielectric background is exchanged for a multipolar charge distribution in the channel, accounts for dielectric reorganization of the solvent [9–11]. Because this perturbation involves processes occurring in a uniform dielectric background, it would appear that there is no Born contribution. This is correct as long as the exchanged species (ion and water) have the same radii; however, if their radii differ there is an additional small term in the free energy which can be accurately accounted for by decomposing stabilization into two more steps [60]. The ion–water exchange takes place without a radius change creating an intermediate "water" of modified cavity size; the radius change is then dealt with by exchanging this intermediate species for a normal water.

1. Applications: Parameterizing Ion–Water Interactions

The reliability of the SMC approach is crucially dependent on devising reasonable interaction parameters. Here, we describe their determination by computing the free energy of ionic dehydration and contrasting the consequences of two values of $\varepsilon_{\text{background}}$, either 1.8 or 2, and two values of water's hard-core radius, either 1.4 or 1.5 Å. The rationale for the ε choices has already been given. The radius choices correspond to the mean water–water nearest neighbor distance in liquid water and the water–water separation in the dimer, respectively [67]. Instead of exchanging an ion in the dielectric background for a water in

the channel, the third step of the equivalent thermodynamic process of Eqs. (3)–(5) now involves exchanging the ion for an explicit water in a sphere containing a limited number of explicit waters (~40) surrounded by bulk water. Both energies, Eq. (4) and the analog to Eq. (5), depend on the choice of $\varepsilon_{\text{background}}$ and the water hard-core radius. Table 1 presents dehydration energies for six hypothetical ions of various hard-core radii; these are compared with "experimental" data, estimated from the absolute dehydration free energies for K^+, Rb^+, Cs^+, F^-, Cl^-, and Br^-, assuming Pauling's ionic radii [61]. An $\varepsilon_{\text{background}}$ of 2 is clearly preferable to the choice of 1.8; both water hard-core radii yield acceptable free energy values for cations, but the overall agreement is better using a water radius of 1.4 Å. Only for the Br^- analog ($R = 1.95$ Å) are disagreements significantly larger than the computational uncertainty.

It should be stressed that the SMC parameterization procedure is very different from standard Born model analysis where an ion of assigned radius is embedded in a uniform continuum dielectric with bulk permittivity. Here, the ion is fully solvated by the model water, and the dielectric constant reflects the solvent's electronic properties. The structural component of dielectric reorganization is treated explicitly.

2. Applications: Permeation Energetics in KcsA

The great strength of SMC modeling is its flexibility. KcsA provides an excellent demonstration system. Structural features can be added sequentially to determine which have significant co-operative influences on $\Delta G_{\text{permeation}}$. The effect that mobility of portions of the peptide distant from the channel ion transport domain have on $\Delta G_{\text{permeation}}$ can be addressed separately, in effect providing a measure of how such motions alter the channel protein's effective ε. The extent to which water, in the channel mouth, in the central cavity, or in the conducting system's intracellular channel connecting the protein's inner mouth to the central cavity, can be described in continuum terms is readily investigated. The possible influence of filter radius on $\Delta G_{\text{permeation}}$, important for understanding how the wider filter can be selective [29], is accessible to study. We can use Fig. 1 to illustrate how some of these questions can be approached by addition of layers of complexity.

The model, in its simplest form, has only 21 mobile features, the ion(s) and waters within the filter and the carbonyl oxygens that form the binding pockets [11]. The carbonyl carbons, the termini of the oriented α-helices, and the various charged groups explicitly

TABLE 1 Dehydration Free Energies (in kJ mol^{-1}) for Ions of Various Size and Polarity as Functions of Water's Hard-Core Radius, R, and Background Dielectric Constant, ε[a]

Ion properties[b]		$\varepsilon = 2$		$\varepsilon = 1.8$		
Radius (Å)	Valence	$R = 1.4$ Å	$R = 1.5$ Å	$R = 1.4$ Å	$R = 1.5$ Å	"Experiment"
1.3	+1	356 ± 14	345	339	371	351
1.5	+1	313 ± 12	320	309	314	317
1.7	+1	292 ± 11	295	275	285	305
1.3	−1	436 ± 9	428	444	453	445
1.8	−1	304 ± 5	294	279	283	309
1.95	−1	265 ± 5	265	264	260	280

[a] See text.

[b] Computational uncertainties are only listed in the first column; they are essentially independent of ε and R.

treated are immobilized. The model geometry [11] is derived from the x-ray structure. The aqueous cavity is presumed to be a continuum, filled with permittive, high ε, water. The large diameter but thin extracellular mouth is assumed to be filled with essentially immobilized water, in effect forming a low ε Helmholtz layer [68]. There is no water-filled connector extending from the central cavity to the channel's inner mouth. All these are features that can be modified or turned on and off individually, or are restrictions that can be lifted. In Fig. 1, sites 2–5 are the physiologically important ones, equivalent to those found fully or partially occupied in the x-ray structure [5]. Three of them have rough electrophysiological equivalents, identified from single-channel conductance measurements: sites 2 and 4 represent the "outer lock-in" and "enhancement" sites, respectively [27] and site 5 approximates the Ba block site [69]. Site 3 corresponds to the location of the filter's explicit water [5].

Consider first the role of the central cavity. Its major purpose is to stabilize an ion near the center of the membrane [5,49]. Might it have some secondary influence on permeation? Does the cavity stabilize filter ions as well as single file water or as bulk water? Does it isolate the filter from the channel's low ε intracellular domain? How reasonable is the continuum description of the cavity? Would filter energetics be very different in an open channel? To address these questions we limit consideration to ion–water interaction and treat five variants from the default model geometry [11]:

1. Fill the cavity with explicit waters.
2. Vary the cavity radius, keeping overall system width constant.
3. Eliminate the cavity, replacing it by single file waters.
4. Approximate the open state by creating contact between the cavity and the intracellular region, either by shrinking the overall system width or by constructing a water filled connecting tube.

Using the SMC energy decomposition, Eqs. (3)–(5), only the stabilization term is affected by the changes outlined. Thus, we can answer these questions by focusing on that term only, and base conclusions on a hypothetical monovalent ion with the same hard-core radius as water, i.e., a cation intermediate between K^+ and Rb^+. Results are presented in Tables 2–4, for which the computational uncertainties in the energies are $\pm$ 1 kJ mol^{-1}.

Table 2 treats various modifications of the cavity, either filling it with explicit water or varying its radius. These modifications noticeably affect the stabilization free energy only at site 5, adjacent to the cavity. Clearly the high ε, continuum cavity approximation adequately describes the system except at site 5. Table 3 illustrates that, if the filter

TABLE 2 Effect of Cavity Size and Cavity Description[a] on Monovalent Cation Stabilization Free Energies, Eq. (5), for Single Occupancy of Sites of Model Filter (Fig. 1)

Geometric properties		Explicit waters	Stabilization energies (kJ mol^{-1})				
Width (Å)	R_{cavity} (Å)		Site 1	Site 2	Site 3	Site 4	Site 5
49	5	File-5, Cavity-0	−71	−65	−51	−51	−48
49	5	File-5, Cavity-20	−70	−64	−51	−52	−52
49	8.5	File-5, Cavity-0	−71	−65	−53	−54	−55
49	0	File-5, Cavity-0	−70	−63	−50	−47	−37

[a] See text.

TABLE 3 Effect of Intracellular Channel Geometry[a] on Monovalent Cation Stabilization Free Energies, Eq. (5), for Single Occupancy of Sites of Model Filter (Fig. 1)

Geometric properties		Explicit waters	Stabilization energies (kJ mol^{-1})				
Width (Å)	R_{cavity} (Å)		Site 1	Site 2	Site 3	Site 4	Site 5
49	5	File-5, Cavity-0	−71	−65	−51	−51	−48
41	5	File-5, Cavity-0	−71	−65	−51	−52	−49
33	5	File-5, Cavity-0	−72	−66	−53	−54	−53
49	Tube[b]	File-5, Tube-72	−71	−64	−52	−54	−56

[a] See text.
[b] See text and Fig. 1.

geometry is unaltered, transition to an open state can have little effect on ion energetics in the filter itself, again with the exception of site 5. Table 4 compares the stabilizing effect of the cavity with that of hypothetical single file waters and shows that just one single file water is sufficient to compensate for the whole water-filled cavity, underscoring the exceptional stabilizing influence of linear dipolar arrays [70,71].

The overall picture is clear. The cavity did not evolve in order to stabilize monovalent filter ions; more single file waters would do this task better. It does have a real effect on ionic stability at site 5, roughly the Ba block site [69]. Since ion–cavity interaction arises from image forces, quadratically dependent on ionic valence, the site 5 interactions would be four times more effective in stabilizing a divalent Ba than a monovalent alkali cation and may play an important role in determining the site of the block. The cavity effectively isolates the filter from the low ε, interior side of the channel assembly. Without a change in filter geometry, transition to the open state could only marginally alter filter energetics.

Just as we have separated out the influence that the cavity has on ions in the filter, we can ask how the various electrical sources included in the model of the peptide affect the ion's permeation free energy. Assuming that joint effects do not alter the cavity size, this can also be answered by computing stabilization free energies. Again considering (hypothetical) single occupancy we can separately assess the influence of:

TABLE 4 Effect of Replacing Cavity by Single File Waters[a] on Monovalent Cation Stabilization Free Energies, Eq. (5), for Single Occupancy of Sites of Model Filter (Fig. 1)

Geometric properties		Explicit waters	Stabilization energies (kJ mol^{-1})				
Width (Å)	R_{cavity} (Å)		Site 1	Site 2	Site 3	Site 4	Site 5
49	5	File-5, Cavity-0	−71	−65	−51	−51	−48
49	0	File-5, Cavity-0	−70	−63	−50	−47	−37
49	0	File-6, Cavity-0	−70	−64	−51	−51	−55
49	0	File-7, Cavity-0	−71	−65	−52	−54	−59
49	0	File-8, Cavity-0	−71	−65	−53	−55	−61

[a] See text.

1. Bulk and cavity water
2. Single file water
3. The binding pocket carbonyls
4. The oriented α-helices
5. The ^{80}Asp (aspartate) residues near the extracellular mouth

Figure 2 describes each feature's contribution to the stabilization free energy, Eq. (5), for the channel occupied by the hypothetical K^+/Rb^+ hybrid ion described above. Additionally, it indicates the extent to which there is any co-operativity (defined as the difference between the influence of all sources collectively and their contributions individually) in this model of the system, where only the ion, waters, and carbonyl oxygens are mobile. Here, the cavity is presumed to be ion free.

With this model, the total stabilization energy is ~200 kJ mol^{-1}, which compensates for ~60% of the ionic dehydration energy. Attraction to the dielectric background (bulk and cavity water) is strongest at the sites near the two boundaries, with bulk water twice as effective. Stabilization by single file waters is complementary, being strongest in the filter interior where the ion has two single file neighbors. Net stabilization by waters of all kinds (bulk, cavity, and single file) varies from ~20 to ~30 kT. The rest of the dielectric stabilization is dominated by ion–helix and ion–carbonyl interactions. For filter sites nearest the cavity, interaction with the α-helices dominates since these are very close to the four helices' carboxyl termini each with an effective negative charge of $-0.5e_0$ (with e_0 the charge of an electron). In contrast, the negatively charged carboxylate groups of the ^{80}Asp residues near the peptide–water interface are strongly shielded by nearby bulk solvent, greatly reducing their ability to stabilize filter cations. Co-operativity appears to

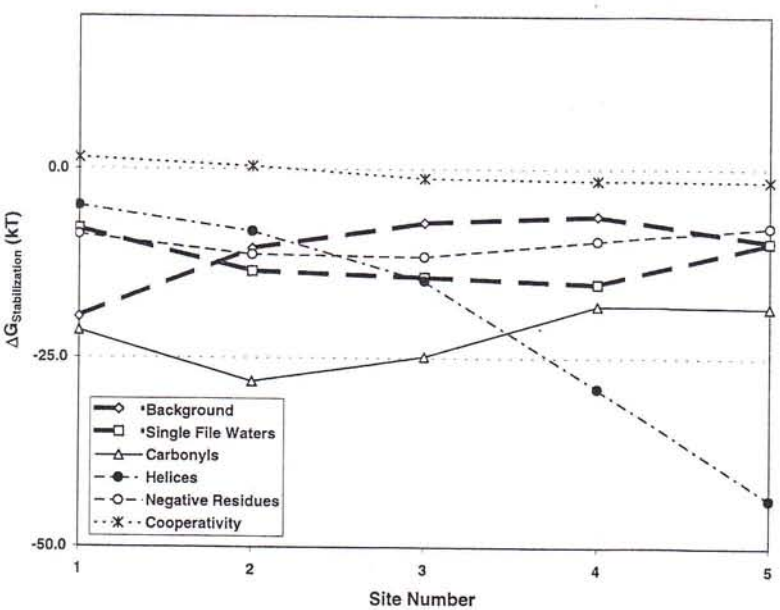

FIG. 2 Individual contributions of the various electrical features (continuum background ◇, single file waters □, binding pocket carbonyls △, oriented α-helices ●, negative residues ○) and of co-operativity (x) to monovalent ion-stabilization energy at various occupancy sites in the model KcsA filter. The water pool does not contain an ion.

make an insignificant contribution to ionic stabilization. These conclusions are basically unaltered if the central cavity is ion occupied. However, there is one interesting change. An ion at site 5 interacts with the single file waters just as well as an ion at site 4; because the fields due to the cavity ion and the site 5 ion reinforce, the single file waters are more favorably aligned than when the cavity is unoccupied.

Finally, consider an example that illustrates the importance of releasing constraints on mobility. The mobile moieties are the ion(s) and waters of the single file, the termini of the α-helices, and the explicit waters in the central pool, which may or may not contain an ion. The carbonyls and the ^{80}Asps are ignored. As long as joint effects do not alter the sizes of the ionic Born cavities, changes in the permeation free energy track changes in $\Delta G_{\text{stabilization}}$. The results are presented in Table 5 [72]. For immobile helices, the rest positions of their charged termini are, by definition, the crystallographic positions. Including mobility complicates matters. The termini's rest positions and the crystallographic positions are not the same, as the structure was determined at ~80–100 K [5]. Rest positions are deduced by requiring that, for crystallographic occupancy (two filter ions and one pool ion), their mean thermal locations at 100 K reproduce the crystallographic data; the force constants are deduced from MD modeling [41]. The data of Table 5 may appear counterintuitive. Because rest positions change, including mobility need not imply increased ion–channel interaction. For immobile modeling, the rest positions of the carboxyl termini are very close to the inner sites, 4 and 5. With mobility included, the rest positions move away from these sites. At all sites, incorporating mobility *decreases* the stabilization energy, the effect being more pronounced at the inner sites. While qualitatively independent of pool occupancy, the effect is amplified for the occupied pool. Naturally, for a specific set of rest positions, energy always decreases when mobility is permitted. Thus, we find that: co-operative effects may be greater than suggested by the primitive model; their sign cannot be predicted with certainty; and treating mobility self-consistently may have surprising consequences.

How dependent these various observations are on model limitations is an open question. Assuming that only the filter contents and the carbonyl oxygens are mobile is quite restrictive; helix terminus mobility has a considerable influence on co-operativity. Since solvent reorganization is the physical basis for dielectric stabilization, we may expect that the mobility of the carbonyl carbons also matters. This is especially true for KcsA, where the filter contents and their surrounding carbonyl oxygens are very tightly packed, so that the oxygens appear very immobile, with mean deflections from their equilibrium

TABLE 5 Effect of Helix Terminus Mobility[a] on Monovalent Cation Stabilization Free Energies, Eq. (5), for Single Occupancy of Sites of Model Filter (Fig. 1)

Geometric properties		Explicit waters	Stabilization energies (kJ mol^{-1})				
Width (Å)	R_{cavity} (Å)		Site 1	Site 2	Site 3	Site 4	Site 5
49	5	File-5, Cavity-0	−71	−65	−51	−51	−48
49	0	File-5, Cavity-0	−70	−63	−50	−47	−37
49	0	File-6, Cavity-0	−70	−64	−51	−51	−55
49	0	File-7, Cavity-0	−71	−65	−52	−54	−59
49	0	File-8, Cavity-0	−71	−65	−53	−55	−61

[a] See text.

orientations of ±3°. Permitting carbonyl carbon motion might markedly unfreeze the oxygens, with possibly significant energetic consequences. These are unpredictable since, to treat thermal motion self-consistently, the atomic rest positions must first be deduced. Of equal interest is explicit solvent in the outer mouth of the filter and its ability to shield the filter contents from the electrostatic influence of ^{80}Asp residues.

III. MEMBRANE INFLUENCES ON GATING AND CHANNEL STABILITY

In their functional forms, channel-forming proteins (or peptides) are embedded in membranes, specifically in lipid bilayers. This implies that lipids affect the proteins' ability to perform their functions by allowing them to form the channel. Changing the membrane composition may affect the protein's affinity to the membrane, and thereby influence its ability to act as an ion-transport catalyst. An illustrative example is the channel formed by dimerizing gramicidin-A (GA). The coupling between GA monomers and the membrane is due primarily to a lipophilic interaction between the peptide's apolar side chains and the membrane's lipid core. In this system the gating process is especially simple. It occurs when monomers on opposite sides of the membrane, each attached to water at the interface by means of its tryptophan residues, diffuse along the surfaces and, colliding, self-assemble and form the membrane-spanning dimer. This creates a highly conductive and comparatively simple ion channel with well-established properties (see Ref. 73 for a comprehensive review). Its stability depends on bilayer composition. Quite importantly, it has been shown that chemical specificity is a relatively insignificant influence on protein–lipid interaction [74–76]. Much more important are the membrane's general physical characteristics, such as its hydrophobic thickness and elastic moduli.

More generally, channel gating requires a conformational change, where mechanical coupling to the membrane may affect either kinetics or equilibria. The clearest cases of membrane involvement arise in self-assembly of small polypeptides, when channels form from peptide monomers of a size comparable to phospholipid molecules [76,77]. In GA the channel lifetime, τ, depends on the membrane's mechanical properties [76]. Alamethicin forms channels with a wide range of conductances, reflecting different oligomerization states; the population equilibrium correlates with changes in the membrane's mechanical properties [78]. It is thus reasonable to expect lipid–peptide mechanical coupling to be important in gating processes that involve the self-assembly of small peptides [79] or as in colicin Ia or diphtheria toxin, the translocation of single peptide strands [80,81]. Where larger, already assembled structures are involved, the gating machinery is likely to be isolated from the surrounding membrane. Thus, there are only a few instances where lipids are known to affect gating kinetics and/or equilibria and the mode of coupling is unclear. Equilibria in rhodopsin is sensitive to changes in acyl chain saturation [82]. Doping membranes with phosphatidylino-sitol-y,5-bisphosphate alters activation in an inward rectifier potassium channel [83] and inactivation of a Na/Ca exchanger [84].

In this section we only discuss the "ultimate gating event," i.e., membrane effects in forming and breaking the conductive GA channel. Our focus here is the elastic influences arising from perturbation of the membrane's thickness in contact with the insertion.

A. Theoretical Background: Elastic Plates and Shells

The elastic problem of a membrane with an insertion is very similar to some classical problems of mechanical engineering in the theory of elastic plates and shells. We first give

a brief review of those problems to provide a necessary background for the discussion of the membranes.

1. Equilibrium Equations

The free energy of a bent plate is [85,86]

$$F_{\mathrm{pl}}^{\mathrm{bend}} = \int b\,[\,(\Delta u)^2 + 2(1-\sigma)T(u)\,]\mathrm{d}f \tag{7}$$

the coefficient b is called the *flexural rigidity* or *cylindrical rigidity* of the plate, $u(x, y)$ is the (small) vertical displacement of its surface, σ is Poisson's ratio, $\Delta \equiv \partial^2/\partial x^2 + \partial^2/\partial y^2$ is the Laplace operator, $T(u) \equiv (\partial^2 u/\partial x \partial y)^2 - \partial^2 u/\partial x^2\ \partial^2 u/\partial y^2$, and $\mathrm{d}f = \mathrm{d}x\mathrm{d}y$.

The natural extension of this model, more closely corresponding to the description of membranes, is the so-called "floating plate" [86]. In a sense this is like a pontoon bridge. Different parts of the floating plate experience deviations $u(\mathbf{r})$, from the flat arrangement opposed by a restoring "Archimedes force," $-au(\mathbf{r})$. In this case the "elastic constant" a depends on the density of the supporting liquid. The total energy is now

$$F_{\mathrm{pl}} = F_{\mathrm{pl}}^0 + \int au(\mathbf{r})^2\mathrm{d}f \tag{8}$$

(in the literature a is also called the *modulus of the foundation*). This equation contains both "bending" and "compression" components which are also the most important contributors to the membrane deformation energy. Although their origin in lipid bilayers is different (e.g., compression is due to steric interaction between the hydrocarbon tails of lipid molecules opposing the thickness fluctuations), the mathematical analogy provides the bridge between these distinctly different systems. The equation of equilibrium for a plate [the deformational profile $u(\mathbf{r})$] can be derived from the condition that its free energy is a minimum corresponding to the appropriate boundary conditions. To do so, we must calculate the variation of Eq. (8), δF_{pl}. It is important to notice that δF_{pl} can be expressed as a sum of two contributions [85,86]:

$$\delta F_{\mathrm{pl}} = \delta F_{\mathrm{pl}}^{\mathrm{surf}} + \delta F_{\mathrm{pl}}^{\mathrm{edge}} \tag{9}$$

The first term contains an integral over the surface of the plate:

$$\delta F_{\mathrm{pl}}^{\mathrm{surf}} = 2\int \delta u(b\,\Delta^2 u + au)\mathrm{d}f \tag{10}$$

which is the energy variation for the plate subject to the arbitrary surface deformation $\delta u(r)$. The second term is the variation in the energy of the edges of the plate. As such it is proportional to a contour integral along all the boundaries of the plate:

$$\delta F_{\mathrm{pl}}^{\mathrm{edge}} = \oint \mathrm{d}l\left[\delta u\, p(\mathbf{r}) + \frac{\partial \delta u}{\partial \mathbf{n}}\, m(\mathbf{r})\right] \tag{11}$$

with

$$p(\mathbf{r})/2b = \frac{\partial \Delta u}{\partial \mathbf{n}} + (1-\sigma)\frac{\partial}{\partial l}\left[\frac{1}{2}\sin(2\theta)\left(\frac{\partial^2 u}{\partial x^2} - \frac{\partial^2 u}{\partial y^2}\right) + \cos(2\theta)\frac{\partial^2 u}{\partial x \partial y}\right] \tag{12}$$

$$m(\mathbf{r})/2b = \Delta u + (1-\sigma)\left[\sin(2\theta)\frac{\partial^2 u}{\partial x \partial y} - \sin^2(\theta)\frac{\partial^2 u}{\partial x^2} - \cos^2(\theta)\frac{\partial^2 u}{\partial y^2}\right] \tag{13}$$

where $\mathbf{n}$ is the normal to the contour of a boundary and θ is the angle between $\mathbf{n}$ and the x-axis.

In the theory of elastic plates and shells it is sometimes natural to introduce explicitly not only the external forces $g(\mathbf{r})$ acting on the surface, but also external shearing forces Q_n and mechanical moments M_n applied to the edges. The equilibrium conditions are then (see Ref. 86, Section 23)

$$\delta F_{\mathrm{pl}} = \int \delta u g(\mathbf{r}) \mathrm{d}f + \oint \mathrm{d}l\, \delta u \mathbf{Q}_{\mathrm{n}}(\mathbf{r}) + \oint \mathrm{d}l\, \frac{\partial \delta u}{\partial \mathbf{n}} \mathbf{M}_{\mathrm{n}}(\mathbf{r}) \tag{14}$$

Further on we limit consideration to situations where a membrane is perturbed on its internal boundaries (contacts with peptides) and no other external forces are present: $g(\mathbf{r}) = 0$. This leads to

$$\delta F_{\mathrm{pl}}^{\mathrm{surf}} = 0 \tag{15}$$

and [given that $\delta u(\mathbf{r})$ is arbitrary]

$$b\,\Delta^2 u + au = 0 \tag{16}$$

Similarly, identifying the contour variations in Eq. (14), we find

$$\oint \mathrm{d}l\, \delta u\, [p(\mathbf{r}) - \mathbf{Q}_{\mathrm{n}}] = 0 \tag{17}$$

and

$$\oint \mathrm{d}l\, \frac{\partial \delta u}{\partial \mathbf{n}} [m(\mathbf{r}) - \mathbf{M}_{\mathrm{n}}] = 0 \tag{18}$$

2. Boundary Conditions

The application of Eqs. (17) and (18) depends on the choice of boundary conditions. If Q and M are fixed (denoted as Q, M conditions) on a boundary L, then from Eqs. (17) and (18) it follows that

$$[p(\mathbf{r}) - \mathbf{Q}_{\mathrm{n}}]_{\mathrm{L}} = 0 \tag{19}$$

$$[m(\mathbf{r}) - \mathbf{M}_{\mathrm{n}}]_{\mathrm{L}} = 0 \tag{20}$$

Alternatively, the constraints may be expressed in "geometrical" terms. For instance, the edge of the plate may be "supported" in which case $u|_L = u_0 = \text{const.}$ and/or "clamped" in which case $\nabla u|_L = s = \text{const.}$ With these conditions, $\delta u|_L = 0$ and $\partial \delta u / \partial \mathbf{n}|_L = 0$, so that Eqs. (17) and (18) are automatically satisfied. In what follows we always assume that both $u(r)$ and $\nabla u(r)$ vanish at the external boundary of the membrane, which is associated with areas "infinitely distant" from the insertions:

$$u(\infty) = 0,\ \nabla u(\infty) = 0 \tag{21}$$

For the problems we study, it is impossible to measure or fix the forces acting at the interfaces, and the geometrical approach is the only one that can be used. For instance, as is discussed below, in the contact between a membrane and an inserted peptide, the "hydrophobic matching" condition naturally defines a displacement u_0 rather than the shearing force causing that displacement:

$$u(r_0) = u_0 \tag{22}$$

Here, r_0 is the radius of the inclusion (or the circular hole); implicit to Eq. (22) is cylindrical symmetry, a simplification that we will generally use.

In some studies [e.g., 87–89] the fourth boundary condition required for solving Eq. (16) is chosen by assuming that the slope of the membrane surface at the edge of the inclusion (the contact slope) is fixed:

$$\nabla u|_{\mathrm{L}} = \mathbf{s} \tag{23}$$

which for cylindrical symmetry gives

$$\frac{\partial u}{\partial \rho}|_{r_0} \equiv u'(r_0) = s \tag{24}$$

The constraints of Eqs. (22) and (23) [or Eq. (24)] are denoted as (u, s) boundary conditions.

In other cases, the second boundary condition is chosen by assuming that the moments $M|_L = 0$ [90,91], which leads to

$$m(r)|_{\mathrm{L}} = 0 \tag{25}$$

With cylindrical symmetry, $m(\rho) = \partial^2 u/\partial\rho^2 + \sigma/\rho\ \partial u/\partial\rho$, and the last equation becomes

$$u''(r_0) + \frac{\sigma}{r_0} u'(r_0) = 0 \tag{26}$$

We denote these constraints, Eqs. (22) and (25) [or Eq. (26)], as $(u, M = 0)$ boundary conditions. They imply that after u_0 is fixed, the slope s adjusts to its optimal value. The corresponding value of free energy, $F_{\min}(u_0)$, *is the minimal free energy corresponding to a given* u_0.

It is important to notice that imposing "geometrical" restrictions on the system implicitly suggests that there are external forces acting at the edges of the inclusion (or the hole). For instance, the force acting at the edge of cylindrical hole and conjugate to u_0 is

$$Q = \frac{\delta F(u, s)}{\delta u}|_{\mathrm{s,u=u_0}} = 2\pi r_0 p(r_0) \tag{27}$$

with

$$p(\rho) = \frac{\partial \Delta u}{\partial \rho} = \frac{\partial^3 u}{\partial \rho^3} + \frac{1}{\rho}\frac{\partial^2 u}{\partial \rho^2} - \frac{1}{\rho^2}\frac{\partial u}{\partial \rho} \tag{28}$$

where $p(\rho)$ is to be calculated from the solutions of Eq. (16) with fixed u_0 and s. In the same manner, the mechanical moment conjugate to s is

$$M = \frac{\delta F(u, s)}{\delta s}|_{\mathrm{s,u_0}} = 2\pi r_0 m(r_0)$$

Therefore, for any choice of M and Q one can find corresponding geometrical parameters u_0 and s, while the imposition of geometrical conditions determines the corresponding forces. The choice between two alternative descriptions is simply a matter of convenience.

3. Hertz's and Related Problems

Hertz [92] solved a mechanical problem in which a circular plate bears a single load P at its center $\rho = 0$. This is mathematically similar to our problem, a membrane containing an inserted peptide. Our discussion is based on that of Ref. 86 and covers the extension

treating circular plates (membranes) with a hole. The fundamental problem is to determine the membrane's surface deformation profile, $u(\mathbf{r})$, the solution to Eq. (16) subject to the appropriate boundary conditions; in cylindrical coordinates Eq. (16) becomes

$$u^{(4)} + \frac{2}{\rho}u^{(3)} - \frac{1}{\rho^2}u''(\rho) + \frac{1}{\rho^3}u'(\rho) + \frac{a}{b}u(\rho) = 0 \tag{29}$$

Its general solution can be expressed in terms of Kelvin functions:

$$u = c_1 kei(x) + c_2 ker(x) + c_3 bei(x) + c_4 ber(x) \tag{30}$$

with $x = \rho/\lambda$, where

$$\lambda = (b/a)^{1/4} \tag{31}$$

is the characteristic elastic decay length. Using the conditions Eq. (21), we should set both $c_3 = 0$ and $c_4 = 0$. As a result,

$$u = c_1\, kei(x) + c_2 ker(x) \tag{32}$$

The remaining constants c_1 and c_2 are defined by the boundary conditions at the plate-insertion interface. Numerous solutions to similar problems with cylindrical symmetry are discussed in Ref. 93. For instance, if (u, s) conditions are appropriate:

$$c_1 = \frac{u_0 ker(x_0)' - s\,\lambda\, ker(x_0)}{\Omega(x_0)} \tag{33}$$

$$c_2 = \frac{s\,\lambda\, kei(x_0) - u_0\, kei(x_0)'}{\Omega(x_0)} \tag{34}$$

$$\Omega(x_0) = kei(x_0)\, ker(x_0)' - ker(x_0)\, kei(x_0)'$$

with $x_0 = r_0/\lambda$. Using the $(u, M = 0)$ conditions, Eqs. (22) and (26), we find

$$c_1 = u_0 \frac{r_0\, kei(x_0) + \lambda(1-\sigma) ker(x_0)'}{\Delta} \tag{35}$$

$$c_2 = u_0 \frac{r_0\, ker(x_0) - \lambda(1-\sigma)\, kei(x_0)'}{\Delta} \tag{36}$$

$$\Delta = \lambda(1-\sigma)\Omega(x_0) + r_0 |\mathbf{K}_0(\sqrt{\mathbf{i}}x_0)|^2$$

where $\mathbf{K}_0(\mathbf{z})$ is a modified Bessel function of the second kind. The free energy calculated for the surface deformation profile, Eq. (32), is

$$F = 2\pi\,[\, x_0\,(c_1^2 + c_2^2)\sqrt{ab}\;\Omega(x_0) + (1-\sigma)\, b\, u'(r_0)^2] \tag{37}$$

Instead of solving the Hertz problem directly, with the load P fixed in the center, we fix $u(0) = u_0$, use the solution for the $(u, M = 0)$ conditions [Eqs. (35) and (36)], and only then express u_0 in terms of P. In the limit $r_0 \to 0$, $c_2 \to 0$, and

$$c_1 \to \frac{u_0}{kei(0)} = \frac{4u_0}{\pi}$$

Noticing that in the same limit $x_0\Omega(x_0) \to \pi/4$, we find for the energy:

$$F_{\text{Hertz}} = 8u_o^2\sqrt{ab} \tag{38}$$

where the second term in Eq. (37) drops out because as $r_0 \to 0$, $u'(r_0) = u'(0) = 0$.

The load P, conjugate to the displacement u_0 and acting at the center of the plate, can be found as:

$$P = \frac{\partial F_{\text{Hertz}}}{\partial u_o} = 16 u_o \sqrt{ab}$$

The same result could be derived using the definition of Eq. (28) for $p(\rho)$ and the condition of force balance [86]:

$$P = Q = 2\pi r_0 p(r_0)|_{r_0 \to 0} \text{ [see Eq. (27)]}$$

It is interesting to notice, based on Eq. (38), that, in relation to lifting its central point, an infinite membrane behaves like a spring with the effective force constant:

$$K_{\text{spr}}^{\text{Hertz}} = 16\sqrt{ab} \tag{39}$$

B. Membranes with a Single Insertion

Membranes are self-assembled bilayers of amphiphilic molecules. When a protein is inserted into a membrane, the thickness of the membrane adjusts to match the thickness of the hydrophobic region of the inclusion in order to minimize the exposure of the nonpolar parts to the aqueous environment. Thus, the natural choice for a boundary condition is to define a perturbation of the membrane thickness at the interface:

$$2u_0 = h_0 - l_h \tag{40}$$

where h_0 and l_h are the unperturbed hydrophobic membrane thickness and the hydrophobic length of the channel, respectively [87,88] (see Fig. 3).

The possibility of an exact hydrophobic match, Eq. (40), has been analyzed recently [89]. The elastic energy of matching should be compared with the free energy of hydrophobic mismatch, i.e., the increase in surface energy due to the contact of the nonpolar lipid tails with water. While the elastic energy is proportional to u_0^2, the mismatch energy is a linear function of u_0. This means that for a sufficiently large value of u_0 the membrane

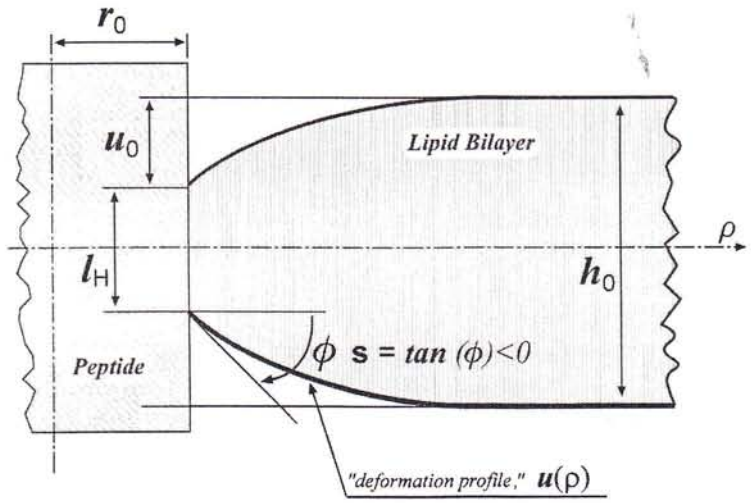

FIG. 3 Schematic diagram of the peptide–membrane interface.

would prefer to remain undeformed, gaining some mismatch energy instead. The estimate shows that the matching condition, Eq. (40) is likely to be fulfilled for $u_0 \leq 2.65$ Å, and that for larger u_0 some slippage or incomplete matching may occur. This means that $u(r_0)$ for larger mismatches may be smaller than the u_0 defined by Eq. (40). This important notion should be kept in mind, although throughout our discussion we assume that the hydrophobic matching condition is fulfilled.

Being perturbed at the interface, the membrane profile $u(r)$ adjusts itself gradually to minimize the elastic energy. The corresponding free energy of membrane deformation can strongly affect both protein conformation and protein function. For the GA insertion considered below, these effects manifest themselves through the influence of membrane parameters (elastic constants, thickness of the bilayer) on the lifetime τ of the ion channel, i.e., the dissociation of GA dimers into separate monomers.

1. Elastic Description of Membranes

In theoretical studies of these phenomena, membranes are traditionally described by means of the "smectic bilayer" model [76,87,88,94,95], although other approaches have also been used [96,97]. The original model was designed for the description of smectic liquid crystals [98]. The elastic energy in such systems depends on both the positions and orientations of their constituent molecules. The corresponding degrees of freedom are described through the displacements $u(\mathbf{r})$ and a director $n(\mathbf{r})$. Under the assumption that deformation is smooth enough, and that the director adjusts to the local normal to the surface, the deformation energy can be expressed in terms of the $u(\mathbf{r})$ alone. Adapted to the description of bilayers, the energy in this model consists of three contributions.

1. Splay ("bending" or "curvature" energy):

$$F^{\text{bending}} = \int \frac{Kh_0}{2} (\Delta u)^2 \mathrm{d}f \tag{41}$$

where K is the bending (splay) constant related to the curvature elastic modulus K_c ($K_c = Kh_0$). Formally, Eq. (41) can be derived from the plate bending energy [Eq. (7)] by the substitutions $b \to Kh_0/2$, and $T \to 0$.

2. Compression–stretching energy:

$$F^{\text{stretching}} = \int \frac{2B}{h_0} u^2 \mathrm{d}f \tag{42}$$

where B is the stretching modulus.

3. Surface tension contribution:

$$F^{\text{tension}} = \int \frac{\gamma}{2} (\nabla u)^2 \mathrm{d}f \tag{43}$$

where γ is the surface tension coefficient.

The issue of surface tension is quite controversial [99–107]. Fortunately, existing estimates [76,88] and experimental data [108] show that, even when included, this contribution is not important. For this reason we omit the surface tension term throughout the remainder of this paper.

Considering only the first two terms, and comparing Eqs. (4) and (42) with Eqs. (7) and (8), we find that the problem of a membrane with an insertion is equivalent to that of a floating plate [Eq. (16)], assuming the correspondences:

$$a = \frac{2B}{h_0},\ b = \frac{Kh_0}{2},\ \text{and}\ T[u] = 0 \tag{44}$$

In addition, the surface forces and moments, Eqs. (12) and (13), must be substituted by

$$p(\mathbf{r}) = \frac{\partial \Delta u}{\partial \mathbf{n}} \tag{45}$$

$$m(\mathbf{r}) = \Delta u \tag{46}$$

2. Elastic Problem for a Single Cylindrical Insertion

The elastic problem for a membrane with a cylindrical insertion, accounting for both compression and splay contributions, was first studied by Huang [87]. In this study, Eq. (16) was solved using the (u, s) boundary conditions, Eqs. (22) and (24). The general solution is given by Eq. (32) with the coefficients c_1 and c_2 determined from Eqs. (33) and (34) with the characteristic decay length:

$$\lambda = \left(\frac{Kh_0^2}{4B}\right)^{1/4} \tag{47}$$

In a membrane with a comparatively small stretching modulus λ is large. Conversely, large stretching and relatively low bending constants lead to a small value of λ. This result is easy to understand. If B is large, the most effective way to reduce the energetic cost of a thickness perturbation is for $u(r)$ to decay to 0 as rapidly as possible. If K were negligible, u would have dropped abruptly (with infinite slope). If K is finite but small, the decay is still steep and λ is small. Obviously, if B is comparatively small, $u(r)$ decays smoothly, so that the curvature contribution is small. For the typical solvent-free membrane, λ is close to 10 Å (see below). Interestingly, despite a significant variation in B, K, and h_0, the values of λ are typically found in a narrow range, between ~ 8 and ~ 12 Å. Calculating the membrane deformation energy:

$$F = 2\pi \int_{r_0}^{\infty} [b(\Delta u)^2 + a\, u(\rho)^2]\rho \, \mathrm{d}\, \rho$$

using the general solution, Eq. (32), and the correspondences, Eq. (44), we find [87]:

$$F = 2\, \pi x_0\, (c_1^2 + c_2^2)\sqrt{KB}\, \Omega(x_0) \tag{48}$$

an expression quite similar to that for the plate, Eq. (37).

The results for a GA insertion into a glyceryl mono-oleate (GMO) membrane are illustrated in Figs 4 and 5. The parameters are those used in the literature [87,88]: $B^* = 5 \times 10^{-8}$dyn Å^{-2}; $K^* = 10^{-6}$dyn; $h^* = 28.5$ Å. The hydrophobic length of GA in Eq. (40) is chosen to be $l_h = 21.7$ Å, and its external radius is $r_0 = 10$ Å. From Eq. (40) it follows that $u_0 = 3.4$ Å. The asterisk indicates that these parameters define a "reference" set [76].

Figure 4 demonstrates how the total elastic energy, Eq. (48), and its stretching and bending components, depend on the contact slope s. The coefficients c_1 and c_2 are determined from Eqs. (33) and (34). It is important to notice that in the vicinity of the energy minimum, the stretching contribution strongly dominates bending, while the bending

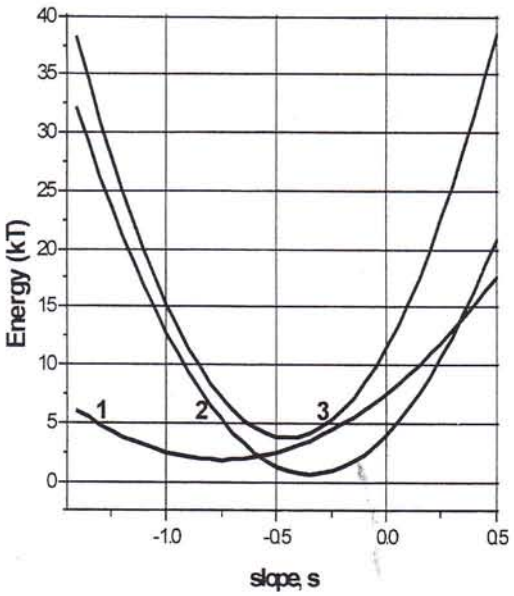

FIG. 4 Elastic free energy (3), decomposed into its stretching (1) and bending (2) components as functions of slope s.

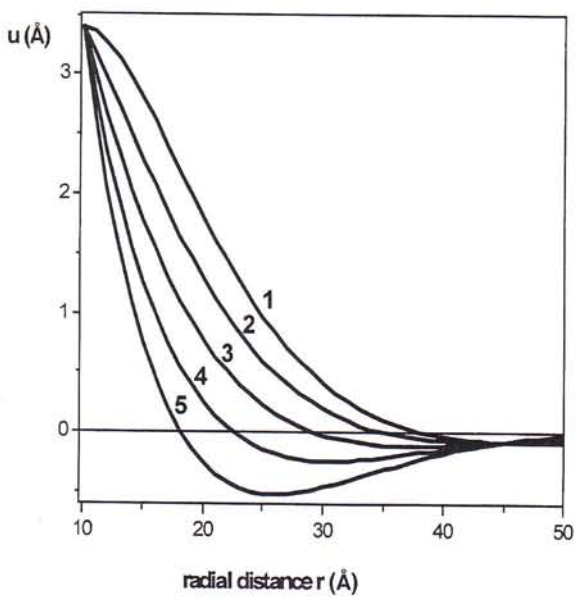

FIG. 5 Membrane deformation profiles for $s = 0$ (1), -0.2 (2), -0.4 (3), -0.6 (4) and -0.8 (5).

energy's s dependence is much sharper. As has already been indicated, the surface tension contribution to the insertion energy is negligible [76,86].

Figure 5 illustrates deformation profiles for various s. An important feature of these curves is their nonmonotonic behavior, which can result (depending on the value of s) in a prominent peak at distances $\sim$ 20–30 Å from the insertion, so that in that region the membrane's thickness exceeds its unperturbed value h_0. In addition to their variation with s, the magnitude of these oscillations also depends on the elastic constants B and K [through the dependence of $u(r)$ on the decay length λ]. These and other properties of the deformation profiles have been discussed in detail in Ref. 76. In a sense, this "overexpansion," in response to thinning of the membrane at the interface, is reminiscent of "overscreening" of electrical charges in electron plasmas or electrolytes [109], when the electrical field in a particular region reverses its direction. These oscillations can be important for membrane-mediated elastic interactions between insertions. They can become more prominent if the discreteness of the membrane (its molecular nature) is taken into consideration [110]. It is interesting to note that the possibility of "overexpansion" was discussed in relation to the problems of elastic plates (the Hertz problem) a long time ago. It was noticed that raising of the loaded elastic plate above its unloaded level is never observed experimentally [86]. It has also been shown that the modified theory of plates, treating them as three-dimensional bodies, does not normally predict such an "anomaly." This does not mean, however, that such behavior is forbidden in soft materials like membranes.

C. Experimental Results: Analysis Using Elastic Models

1. Lifetime of Gramicidin Channels and Linear Spring Model

A release of the elastic energy is considered a major factor in dissociation of gramicidin channels into separate monomers with a corresponding loss of conductance [87,88,111]. The dissociation rate constant k_{diss} can be described as [87,111]

$$\ln\{k_{\text{diss}}\} = -\ln\{\tau\} = -\Delta G/RT - \ln\{\tau_0\} \tag{49}$$

where

$$\Delta G = \Delta G_{\text{int}} + \Delta G_{\text{def}} \tag{50}$$

is the activation energy for channel dissociation, ΔG_{int} is the intrinsic activation energy independent of u_0, and ΔG_{def} is the contribution due to deformation [111]. From the nature of ΔG_{def}, the only part which depends on h_0, one can expect that in a group of similar membranes an increase in the difference between the length of the channel hydrophobic exterior and the thickness of the membrane leads to a higher dissociation rate. This is supported experimentally.

Three groups of membranes have been analyzed: *monoglyceride/squalene* bilayers (thickness changes up to 0.7 nm) [112], *monoglyceride*/n-*hexadecane* bilayers (changes up to 2 nm), and *monoglyceride*/n-*decane* bilayers (changes up to 1.7 nm) [113]. It has been shown that in each group, $\ln \tau$ is a linear function of the membrane thickness h_0. This result naturally leads to a phenomenological "linear spring" model [76,111] for the bilayer deformation energy due to insertion:

$$G_{\text{def}}(u_0) = H(2u_0)^2 \tag{51}$$

where H is the effective spring constant.* It is assumed that dissociation of GA channels occurs abruptly after a certain separation δz is reached between the two monomers constituting the channel. While Huang [87] suggested using $\delta z \sim 0.1$ nm, Lundbæk and Andersen [111] proposed that $\delta z \sim 0.16$ nm would be a better choice for a critical separation for breaking of the hydrogen bonds holding the GA monomers intact. The mismatch dependence of the dissociation rate constant is then given by [111]

$$\mathrm{d}(\ln\{k_{\mathrm{diss}}\})/\mathrm{d}u_0 = 4H\delta z/RT \tag{52}$$

This equation permits expression of the effective spring constant H in terms of the measured slope of $\mathrm{d}\ln(k_{\mathrm{diss}})/\mathrm{d}h_0$. The results depend on the choice of δz. For the monoglyceride/squalene system, $\mathrm{d}\ln(k_{\mathrm{diss}})/\mathrm{d}u_0 \sim 17.8\ \mathrm{nm}^{-1}$ [111]. Assuming $\delta z \sim 0.16$ nm one finds

$$H^{\mathrm{exp}} \sim 69\ \mathrm{kJ\,mol^{-1}nm^{-2}} \tag{53}$$

2. Interpretation of Experimental Data in Terms of Elastic Theory

This result, Eq. (53), posed a challenge to the elastic description of the insertion barrier. For illustration, let us consider the $(u, M = 0)$ conditions. As previously mentioned, the boundary condition corresponds to complete minimization of the elastic energy with u_0 fixed.

The coefficients c_1 and c_2 are defined by Eqs. (35) and (36) from which it follows that

$$c_1 = u_0 \frac{kei(x_0)}{|\mathbf{K}_0(\sqrt{\mathbf{i}}x_0)|^2} \tag{54}$$

$$c_2 = u_0 \frac{\mathrm{ker}(x_0)}{|\mathbf{K}_0(\sqrt{\mathbf{i}}x_0)|^2} \tag{55}$$

Both c_1 and c_2 are proportional to u_0, which leads directly to the linear spring model:

$$F_{\mathrm{min}} = H^{\mathrm{min}}\,(2u_0)^2$$

with the elastic constant for the minimized energy equal to

$$H^{\mathrm{min}} = \frac{4\pi x_0\sqrt{KB}\,\Omega(x_0)}{|\mathbf{K}_0(\sqrt{\mathbf{i}}x_0)|^2}$$

For the GMO parameters this leads to

$$H^{\mathrm{min}}_{\mathrm{GMO}} \sim 19\ \mathrm{kJ\,mol^{-1}nm^{-2}} \tag{56}$$

The corresponding value of the elastic energy induced by the insertion is [88]

$$F_{\mathrm{min}} \sim 4\,kT$$

with the contact slope $s_{\mathrm{min}} \sim -0.45$ (see Fig. 2). As we can see, $H^{\mathrm{min}}_{\mathrm{GMO}}$ is far less than the experimental prediction, Eq. (53).

---

* Note that defined in this way, the spring constant is half its conventional value.

Huang [87] was the first to address this challenge. Instead of minimizing F over s, the equivalent of the $(u, M = 0)$ condition, he suggested treating s as a parameter. Its value, $s = s_{exp}$, was determined by comparison with experiment. As $s_{min} \sim -0.45$ corresponds to the minimum of $F(s)$, any shift of s from this value, either negative or positive, increases H. Huang considered only small $|s|$ and found that $s_{exp} \sim 0$*. This choice has been commonly accepted and apparently justified in a number of later publications [e.g., 76,89,91,111]).

One of the arguments against energy minimization was presented in Ref. 89. It was suggested that total free energy consists of a membrane deformation energy term, $F(s)$, and a boundary energy term, $E_{bd}(s)$. The correct solution for s_{min} should then be obtained from $F'(s) + E'_{bd}(s) = 0$. Although a sensible idea, this suggestion leaves some important questions unaddressed.

For instance, if the contribution E_{bd} were important, it would be unreasonable not to include it directly in the analysis of the membrane-mediated interaction between the insertions, and in the energetics of channel formation. However, this has never been attempted. Also, the interactions responsible for this "surface" contribution cannot be localized at the geometrical surface, but must affect the membrane's properties in the vicinity of the insertion. This poses a question of how valid it is to describe the membrane with Eq. (16), which ignores these interactions. It is well known that even well-defined solid interfaces are actually transition regions where the properties of both phases are strongly modified. This should be even more the case for the soft contacts involving membranes.

D. Nonuniform Membrane Model

Based on these and similar considerations, we decided to attempt to incorporate the interfacial perturbation directly into the membrane model. Hydrophobic interaction with the peptide imposes some limitations on the mobility of the molecules and, consequently, on their ability to readjust. We describe these limitations through the material properties and the membrane elastic constants, and assume that in the vicinity of an insertion they must differ from their bulk values. The decay length of this perturbation must be comparable to the length of lipid molecules. Equating these two characteristic lengths, we reduce the number of parameters to two "surface enhancement factors" for both stretching and bending moduli. As will be seen from our analysis, only the perturbation of the stretching constant has a significant effect on the insertion energetics, which effectively reduces the number of parameters to one.

The idea that membrane elastic constants could be modified by the insertion is not a new one. It was suggested [76,89] that, on the molecular scale involved in the insertion energetics, the elasticity coefficients might differ from their macroscopic values (see also Ref. 114). Furthermore, membranes' material constants are nonlocal [115–117] (see also similar predictions for the interfacial tension [118]), which implies that their behavior on short-length scales differs from the macroscopic limit even for uniform membranes, as has been recently observed experimentally [119,120].

---

* It follows from Fig. 4 that the same increase in energy would also correspond to $s \sim -0.8$. There is no criterion for choosing between these two possible values for s_{exp}. Probably his argument was that a lage negative contact slope would be harder to justify by geometrical (or molecular packing) arguments.

1. Euler–Lagrange Equation

Assuming that elastic moduli K and B depend on r:

$$a(r) = \frac{2B(r)}{h_0},\ b(r) = \frac{h_0 K(r)}{2} \tag{57}$$

we rewrite Eq. (8) for the nonuniform membrane model as

$$F_{\text{nu}} = \int [b(r)(\Delta u)^2 + a(r)u^2(r)]\mathrm{d}f$$

The Euler–Lagrange equation for a membrane with a single cylindrical insertion then takes the form:

$$c_0 u(r) + c_1 u'(r) + c_2 u''(r) + c_3 u^{(3)}(r) + c_4 u^{(4)}(r) = 0 \tag{58}$$

with

$$\begin{aligned} &c_0 = a(r);\ c_1 = \frac{b(r)}{r^3} - \frac{b'(r)}{r^2} + \frac{b''(r)}{r}; \\ &c_2 = -\frac{b(r)}{r^2} + 3\frac{b'(r)}{r} + b''(r);\ c_3 = 2\left[\frac{b(r)}{r} + b'(r)\right];\ c_4 = b(r) \end{aligned} \tag{59}$$

For the nonuniform model, the $M|_L = 0$ condition, Eq. (25) is unaltered, while Eq. (26) is modified to

$$\frac{\partial}{\partial r}[b(r)\,\Delta u]|_{r=r_0} = 0 \tag{60}$$

2. Possible Implications of Nonuniformity

The boundary problem for Eq. (58) was solved [117] using the Shooting Algorithm implemented with Mathematica 4 [121]. Comparison with analytical solutions in the uniform limit demonstrated agreement to within 2% for deformation profiles and to within 5% for the elastic energy.

We are suggesting that the perturbation of B and K, in contact with the insertion, propagates in the membrane for distances λ_c, comparable to the length of lipid molecules themselves, $\sim h_0/2$. For simplicity, we first presume that the relative distance dependence of both stretching and bending moduli can be described by the same transition function:

$$T(r) = 1 + (\theta - 1)\exp\left(-\frac{r - r_0}{\lambda_c}\right) \tag{61}$$

so that

$$a(r) = \frac{2B}{h_0}T(r),\ b(r) = \frac{2K}{h_0}T(r) \tag{62}$$

The coefficient θ accounts for the relative increase in elastic constants at the interface as compared to their bulk values. We shall then consider how independently perturbing the bending and stretching constants affects the elastic energy.

It can be seen from Fig. 6 that a local increase in elastic constants significantly increases the elastic energy barrier. Thus, for GMO a three-fold increase in $E_{\min}$, which would be consistent with the experimental values of the channel lifetimes, requires $\theta \sim 4$. We obtained similar results for ditridecanoyl-sn-glycero-3-phosphocholine (DTPC) and dimyr-

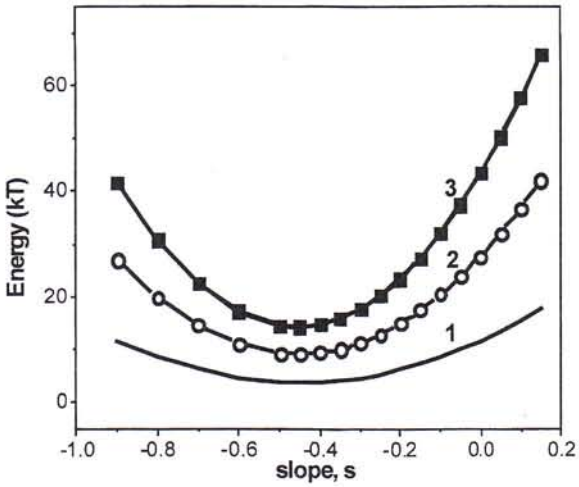

FIG. 6 Elastic energy versus contact slope, s, as a function of the enhancement factor, $\theta_K \equiv \theta_B \equiv \theta$: (1) $\theta = 1$, ——; (2) $\theta = 3$, ○; (3) $\theta_K = 5$, ■.

istoyl lecithin (DMPC) using the literature values of their bulk properties [122] and following Ref. 76, assuming that a reasonable estimate for the energy barrier is given by setting $s \sim 0$ in uniform model calculations. In both cases the enhancement parameter θ is ~ 4.

We have assumed that both K and B are scaled by the same transition function $T(r)$. However, the surface perturbation of these moduli may and must be different. Local increase in K is mainly due to the restricted orientational mobility of the lipid molecules near the inclusion, while variation of B is mainly due to reduced conformational mobility of the "tails" of lipid molecules responsible for the resistance to compression (obviously, these effects are not completely independent). Therefore, a more accurate model must include two surface constants, θ_K and θ_B. To estimate their relative influence we study them independently. In other words, two limits are considered, $\theta_K = \theta$, $\theta_B = 0$ and $\theta_K = 0$, $\theta_B = \theta$. The results of this analysis are presented in Fig. 7.

It is clear that perturbation of the stretching constant (increase in θ_B) has a much greater effect on the elastic energy barrier, $E_{\min}$, than the increase in θ_K. In fact, the perturbation of B alone is responsible for about 80% of the total increase in the elastic barrier. Moreover, if only the bending constant were affected, than the threefold increase in $E_{\min}$ would require $\theta_K \sim 40$(!). These tendencies are illustrated in Fig. 8.

In addition, one can see that θ_B and θ_K drive the optimal slope $s_{\min}$ in opposite directions. Increasing θ_B tends to make $u(r)$ steeper, thus more effectively reducing the stretching energy, while increasing θ_K has the opposite effect. As we can see, the energy barrier is amazingly insensitive to the surface perturbation of the bending modulus. On the other hand, variation of θ_K greatly affects the shape of $F(s)$. Such behavior is similar to that found in the uniform model, where bending mainly influences the s-dependence of the energy, but not the equilibrium energy barrier (see the previous discussion, and Refs 76 and 88).

It should be noted that with $\theta \sim 4$ (the value required to account for the energy barrier to GA dimerization in GMO), the contact slope is $s_{\min} \sim -0.39$. This reduction in s accords with suggestions made previously [76,87]. However, in our approach it is a direct consequence of complete optimization of the nonuniform energy functional.

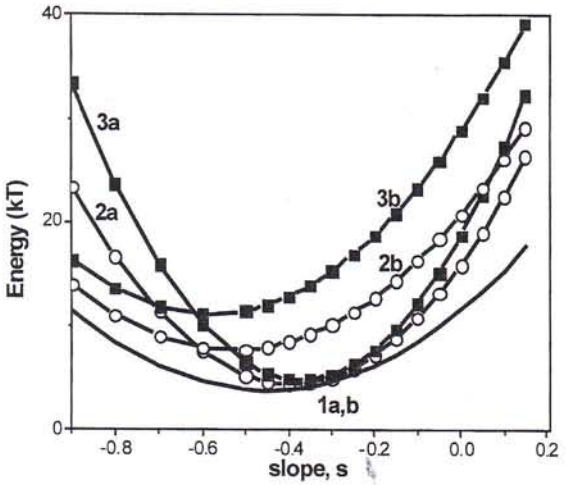

FIG. 7 Elastic energy versus contact slope, s, as separate functions of bending (θ_K) and stretching (θ_B) enhancement factors: (1a,b) $\theta_{B,K} = 1$, —; (2a) $\theta_K = 3$, ○; (3a) $\theta_K = 5$, ■; (2b) $\theta_B = 3$, ○; (3b) $\theta_B = 5$, ■.

Let us now consider how our treatment differs from the conventional approach of using s as an adjustable parameter. We have suggested that there is a nonuniform increase in the membrane elastic constants in the vicinity of the peptide inclusion. Based on this assumption, we allowed the deformation profile to attain its equilibrium slope $s_{\min}$, and found the corresponding energy barrier or, equivalently, the effective elastic constant H. Thus, instead of adjusting s, we have stressed the possibility of local perturbation of the elastic constants. We found that, setting $\theta \sim 4$ yields results equivalent to fixing the contact slope $s \sim 0$ in the uniform model. Even though the conclusions are similar, we think the nonuniform model has some distinct advantages:

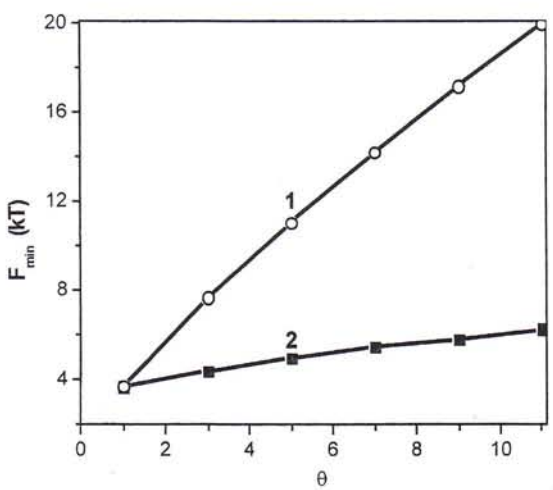

FIG. 8 Energy barrier, $F_{\min}$, as a function of the enhancement factor θ if only: (1) the stretching factor θ_B, ○; or (2) the bending factor θ_K, ■, is perturbed by the insertion.

1. It is widely presumed that in the vicinity of insertion the elastic properties must differ from the macroscopic limit [76,89]. However, this notion has not previously been implemented in a computational model.

2. The argument for fixing the slope requires introducing an additional "surface energy" component [89] which is otherwise not present in the picture. There is a reason to believe that such a perturbation not only influences the contact slope, but also directly affects the barrier and modifies the membrane properties. That is why we think that the surface perturbation should be explicitly incorporated in the membrane model.

3. It is worthwhile formulating a model in terms of material properties that are measurable (or at least, potentially so). For instance, the short-range membrane thickness fluctuations at a point r depend on the averaged values of the elastic constants in its vicinity:

$$< u(r)^2 > \sim \frac{kT}{B_{\text{eff}}(r)}$$

where $B_{\text{eff}}(r)$ is an effective elastic constant averaged in the neighborhood of the point r.

These fluctuations may be studied by neutron scattering, spin labeling, and x-ray scattering techniques. There is also evidence from molecular dynamics simulations that local fluctuations near inclusions are smaller than those in the unperturbed bilayers [123,124].

IV. MEMBRANE-MEDIATED INTERACTION BETWEEN INCLUSIONS

Biological membranes contain large numbers of insertions, e.g., embedded proteins and cholesterols. Interaction between insertions includes direct forces, such as electrostatic and van der Waals, and also interactions mediated by the membrane. Our focus here is on the interactions caused by the insertion-induced elastic deformations in membranes.

A number of studies in this field [97,100,125,126] have considered two contributions to the bilayer energy: molecular stretching/compression and the interfacial tension. Yet others have focused on the membrane's resistance to bending [127,128]. Since the pioneering studies of Huang [87] and of Helfrich and Jakobsson [88] (see also Section III) it was clear that membrane deformation is mostly governed by bending and stretching elasticity. The role these forces play in membrane-mediated interaction between insertions has been considered for two flat insertions [129] and for a two-dimensional hexagonal lattice of cylindrical insertions [90,94]. More recently, this problem has been studied for an ensemble of cylindrical insertions (GA channels) and their aggregation, simulated using a Monte Carlo approach [89].

Here, we describe the problem of two or more cylinders, trying to determine when collective (non pairwise) interactions become important. To do this, we develop a high-precision algorithm for solving the Euler–Lagrange equation, Eq. [58], for several insertions.

A. Finite Difference Approach to Elastic Deformations Caused by Inclusions

The technical problem that arises when several inclusions are present is that the system no longer exhibits cylindrical symmetry. The Euler–Lagrange equation:

$$\Delta[b(x, y)\ \Delta u(x, y)]\ + a(x, y)\, u(x, y) = 0 \tag{63}$$

[the generalization of the cylindrically symmetric representation, Eq. (58)] can still be solved numerically using a finite difference representation [130] on a two-dimensional mesh. We have developed a discretization scheme for solving this equation that can be used for any number of inclusions [131]. The computational domain for a single inclusion is shown in Fig. 9. Since both u and ∇u must be specified at the boundaries, in a finite difference representation this implies that u is constrained at two layers of grid points to satisfy boundary conditions at both the periphery of the computational domain and at the edge of each insertion. At the external edge of the computational domain and at the immediately neighboring points we set $u = 0$, which is equivalent to using the boundary conditions, Eq. (21).

For the boundary conditions at the insertion edges (the circles that are the two-dimensional projections of the included cylinders) we presume that u is fixed: $u|_{\text{circle}} = u_0$. In addition, we constrain the slope s on these circles (in some cases s is not held constant, but varies along the boundary circle with a prescribed functional dependence). These assumptions are implemented through the condition:

$$u(i,j) = u_0 + sd(i,j)$$

for the points (i,j) nearest the circumference both inside and outside the circle. Here, $d(i,j) = r(i,j) - r_0$ is the distance between the point (i,j) and the circumference of the circle and $r(i,j)$ is the distance from that point to the center of a circle. In most cases we chose $u_0 = 3.4$ Å typical of GMO. (More commonly, peptide interaction is studied in thinner membranes, such as dilauroylphosphatidylcholine (DLPC) or dimyristoylphosphatidylcholine (DMPC), corresponding to $u_0 \lesssim 1.5$ Å [89,90,132]. Consequently, our choice of u_0 exaggerates the interactions. However, it does not affect the qualitative results).

We first tested the finite difference technique for a single inclusion, which has a simple analytical representation (in the uniform case) or a cylindrically symmetric, simple numerical solution (the nonuniform case, Section III). We used the approximation of Eq.

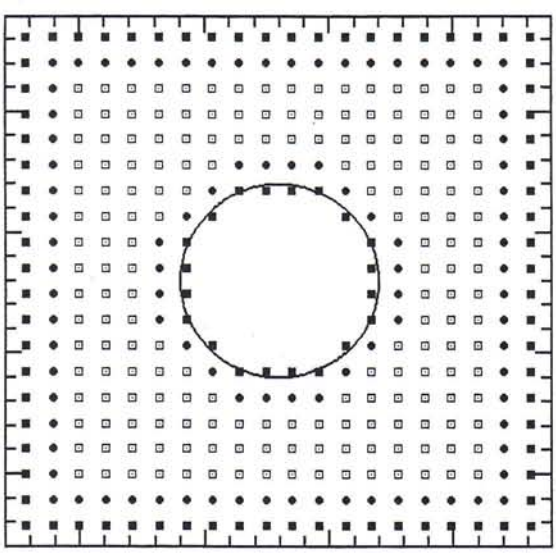

FIG. 9 Schematic view of the computational domain: ■, first layer of the boundary points; ●, second layer of the boundary points; ⊡, interior points of the computational domain.

(62) for the elastic constants. The coefficient θ, Eq. (61), was either equated to 1 (the uniform case) or to 4, which we showed in Section III accounted for experimental lifetimes in the GA channel.

Calculations were carried out for different mesh spacings h (0.5, 1, and 2 Å). Regardless of the value of h, the deformation profiles $u(r)$ were in excellent agreement (to within 2%) with the results described in Section III for both values of θ. However, the total deformation free energy is very sensitive to the choice of h.

Two main sources of error affect the energy integral. First, the surface of distortion is calculated using a finite number of points. Therefore, $u(x, y)$ defined on a discrete set of points is an approximation the precision of which is very sensitive to the choice of h. The bending energy, determined by the second derivatives of u, is especially dependent. Second, in our approach the circles are approximated by zigzag strips of grid points. Given that $u(x, y)$ is both maximal in these regions and its variation is greatest, the alteration of the boundary's shape may introduce another source of error.

Both these errors decrease with refinement of the grid. We found that the grid spacing $h = 0.5$ Å (which is close to the limit of our computational capability) reproduces previous results with good accuracy. Comparison of the deformation free energy profiles as a function of the slope is shown in Fig. 10. The agreement between numerical and analytical data is especially good in the physically most interesting range of slopes (−0.5 to 0.0). The error becomes greater for large negative slopes; for $s = -1.0$ the error in the deformational energy is about 20%.

B. Two Inclusions

We have solved the uniform ($\theta = 1$) elastic problem numerically for two inclusions at various separations, d. We chose $u_0 = 3.4$ Å and varied s. The deformation profiles along the line connecting the centers of two insertions are presented in Fig. 11 for $s = s_{\min}$. As d increases, the well in $u(x)$ becomes deeper. It reaches its minimal value,

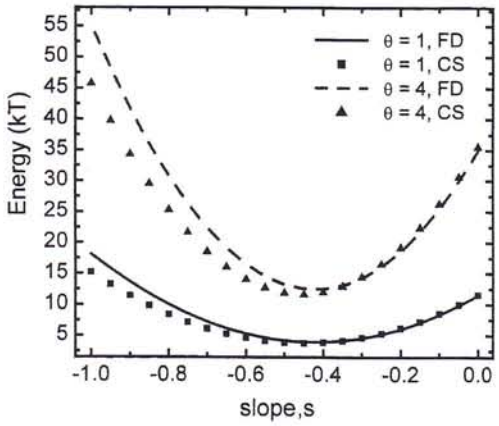

FIG. 10 Deformation free energies versus slope in the uniform ($\theta = 1$) and nonuniform ($\theta = 4$) cases. The results of one-dimensional calculations explicitly utilizing the problem's cylindrical symmetry (CS) either analytically (the uniform case) or numerically (nonuniform model, see Section III) are compared with finite difference (FD) results obtained with the two-dimensional grid.

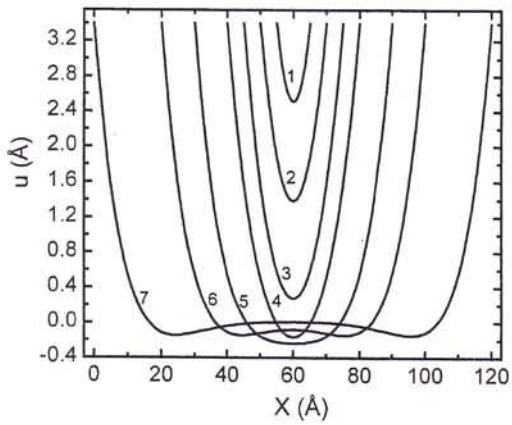

FIG. 11 Displacement profiles between two inclusions along the X axis passing through the centers of the insertions, for different distances between the inclusions: (1) 10 Å; (2) 20 Å; (3) 30 Å; (4) 40 Å; (5) 60 Å; (6) 80 Å; (7) 120 Å.

$u \sim -0.2$ Å, for $d \sim 60$ Å. For larger d it splits into separate minima with a maximum in the middle. Only for $d \gtrsim 80$ Å is the deformation profile reminiscent of the superposed profiles for two independent insertions.

For the relaxed boundary conditions [$s = s_{\min}(d)$] the elastic interaction between two inclusions is repulsive; minimized over s, the interaction free energy decreases with increasing d, Fig. 12. It is interesting to analyze the free energy, $F(d)$, as a function of the contact slope s. We consider the range $0.0 \geq s \geq -0.6$. When $s = 0$, $F(d)$ increases as d increases, i.e., the inclusions attract one another. At large negative slopes the interaction is repulsive. In the intermediate region, $-0.15 \gtrsim s \gtrsim -0.35$, a minimum exists at finite distances between the insertions, which disappears at $s_{cr} \sim -0.35$. In addition, a barrier separates it from the large d region. These results may be physically significant. If the slope s can really be controlled by the insertion, and if it is different for different lipids, one can expect, based on these results, a change in the peptides' clustering behavior (phase transi-

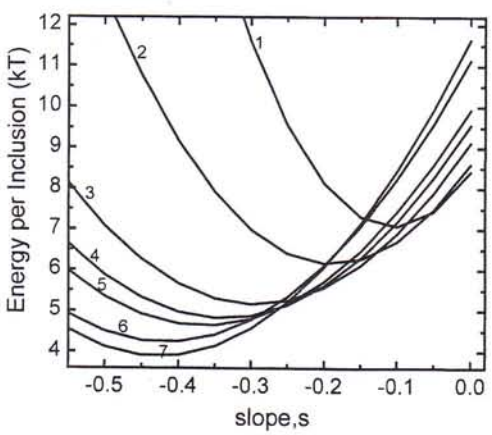

FIG. 12 Elastic energy per insertion for the interaction of two peptides as a function of the contact slope. The distances d are: (1) 1 Å; (2) 2 Å; (3) 5 Å; (4) 7.5 Å; (5) 10 Å; (6) 20 Å; (7) 40 Å.

tion) as the membrane's lipid composition changes. We can expect that similar effects can be formulated in terms of the nonuniform elastic constants, conditions under which θ differs from 1.

We also tested the validity of the assumption that the contact slope remains cylindrically symmetrical when there is more than one inclusion. Actually, along different parts of the insertion surface the membrane's surface may exhibit different equilibrium slopes. One would expect that the perturbation of s should be more significant on the side facing the neighboring insertion. To test this idea, we approximated the slope by a primitive trial function:

$$s(\varphi) = s + s_1 \cos\varphi \tag{64}$$

where s and s_1 are parameters and φ is the "azimuthal" angle. In Eq. (64) the quantity s_1 is added to the average slope s at the segment, $\varphi = 0$, and subtracted at the segment on the opposite side of the circle, $\varphi = \pi$. The free energy of membrane deformation per inclusion as a function of s is shown in Fig. 13 for various s_1. Increasing s_1 initially reduces the free energy. The optimal values of s and s_1 depend on d. This example shows that angular variation of the contact slope may play some role in the interaction between the insertions. However, due to the restricted trial function that we introduced, this only provides a crude initial estimate. Further analysis requires either using a more advanced set of trial functions, or the solution of the $(s, M = 0)$ boundary problem.

C. Many-Body Effects in Membrane-Mediated Interaction Between Insertions

We have shown that, minimized with respect to the contact slope, the interaction between two insertions is repulsive. On the other hand, the interaction involving a larger numbers of insertions may become attractive. This has been observed in a model system of two interacting flat walls [129], which can approximate the interaction between two parallel arrays of insertions. Similarly, an attractive region is present in the interaction free energy for a two-dimensional array of cylindrical inclusions [90,94]. Clustering was also seen in

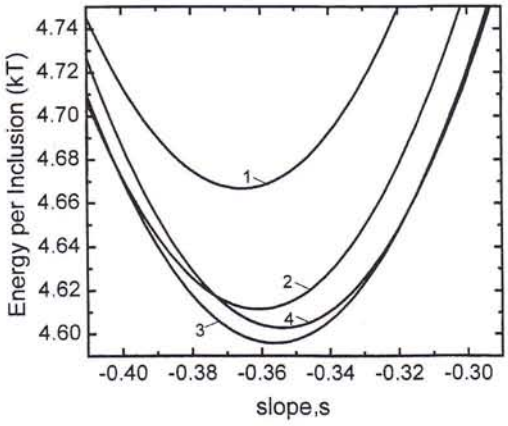

FIG. 13 Deformation free energy per inclusion for two inclusions versus average slope s, with asymmetric boundary conditions; distance $d = 10$ Å. The slope anisotropy parameter s_1 are (1) 0.0; (2) 0.2; (3) 0.4; (4) 0.5.

the Monte Carlo modeling of an ensemble of inclusions [89]. These predictions raise the issue of multiparticle effects in membrane-mediated interaction. Here, we compare the results for systems constituted of two, five, and seven cylindrical insertions.

First, we consider five inclusions, with one at the center and four at the vertices of a square. Figure 14 demonstrates how the deformation free energy per inclusion depends on the contact slope for several distances d between the central peptide and its neighbors (d is the radial distance between the outer surfaces, so that $d = 0$ corresponds to direct contact). For the minimized energy, there is no attraction. However, it differs quantitatively from that seen when only two inclusions are present (Fig. 12). The free energy for five insertions is much less dependent on d. As d decreases from 10 to 1 Å the energy increase per inclusion is only 0.4 kT compared to 2.5 kT for the case of two inclusions.

We have also considered seven inclusions, with one at the center and six at the vertices of a regular hexagon. A contour map of the distortion field is shown in Fig. 15. At the separation illustrated, $d = 15$ Å, the minimum in the free energy occurs for a slope of $s = -0.35$. The closely packed contours near the boundaries of the inclusions demonstrate steep distortion gradients. As is seen from our calculations, seven inclusions can form a stable aggregate. The free energy profiles demonstrating this effect are shown in Fig. 16. They indicate that the attractive region is separated by a barrier from the repulsive one. The shape of the curves is similar to some of the predictions of [90,94] for a two-dimensional hexagonal lattice, where a slightly different elastic membrane model has been used. Our approach does not rely on a Wigner–Seitz type approximation reducing the two-dimensional problem to a one-dimensional (cylindrically symmetric) one. Thus, it has the potential of being able to treat general configurations and arbitrary numbers of insertions, and to model their aggregation. In this sense it is similar to that described in Ref. 89, but our method is more accurate (the grid spacings can be roughly eight times smaller, which could be critical for the evaluation of energy integrals) and has the potential for treating a nonuniform model.

Similar to the case with two insertions, the free energy behavior changes if the slope s is fixed. Again, at small $|s| \sim 0$, the interaction is attractive (see Fig. 17), while at large negative slopes, $s \lesssim -0.4$, it is repulsive. The intermediate region corresponds to nonmonotonic sigma-type curves. It is interesting that, in agreement with previous results [89], at

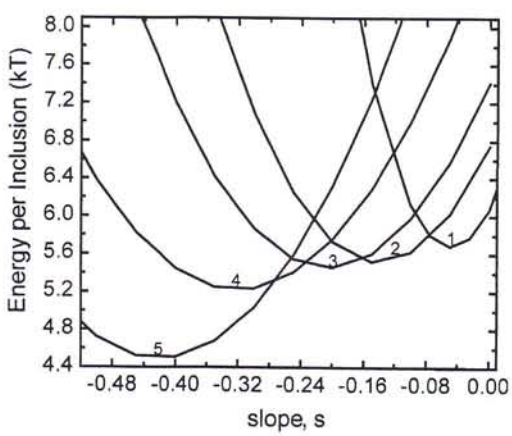

FIG. 14 Deformation free energy (per insertion) versus slope s for five insertions. The distances d are (1) 1 Å; (2) 3 Å; (3) 5 Å; (4) 10 Å; (5) 20 Å.

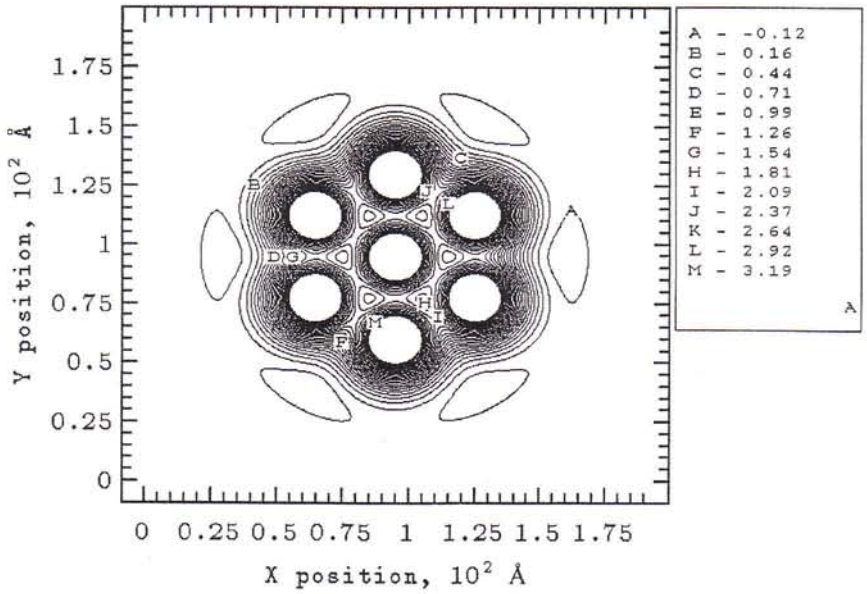

FIG. 15 Distortion field for seven insertions, one at the center and six at the vertices of a regular hexagon. The distance between the surfaces of the neighboring insertions is $d = 15$ Å; the contact slope $s = s_{\min} = -0.35$.

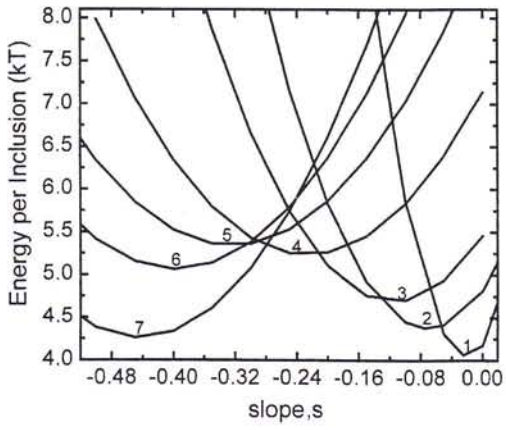

FIG. 16 Elastic energy per inclusion for seven insertions as functions of the contact slope s. The distances d between the neighboring insertions are: (1) 1 Å; (2) 3 Å; (3) 5 Å; (4) 10 Å; (5) 15 Å; (6) 20 Å; (7) 30 Å.

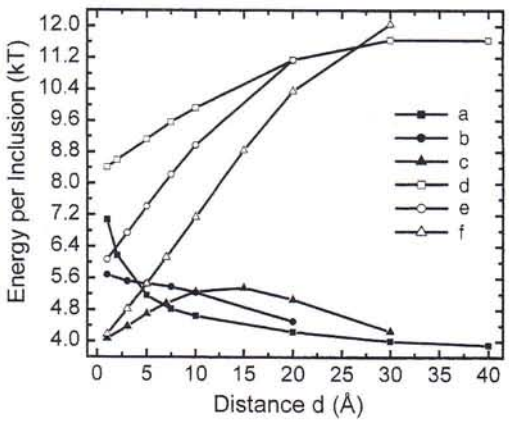

FIG. 17 Deformation energy per inclusion versus the distance d, for the optimized contact slope s_{min}: (a) two inclusions; (b) five inclusions; (c) seven inclusions and for the contact slope $s = 0$: (d) two inclusions; (e) five inclusions; (f) seven inclusions.

larger concentrations (seven insertions, small d) the equilibrium s_{min} shifts towards $s \sim 0$. However, in no way can this serve as an argument for fixing $s \sim 0$ for a single (isolated) insertion.

V. SUMMARY

The semimicroscopic (SMC) method outlined in Section II provides a middle ground between microscopic and mesoscopic approaches to understanding free energy profiles of ions permeating transmembrane channels. By focusing on a limited set of "critical interactions," determination of the free energy profile for a solvated biomolecule can be determined very efficiently. Ion-induced solvent reorientation is described rigorously, including all long-range electrostatic contributions. We presented a simple model force field for ionic hydrates with intuitively reasonable parameters; SMC ionic Born radii are roughly equal to their physical crystal radii. We then considered the physiologically important KcsA K-channel. Decomposition of the influence that individual structural features have on ion stabilization in the narrow filter showed that:

1. The central water cavity (basically designed to stabilize cations in the cavity) helps stabilize ions at the cavity–filter boundary, which may account for the location of the barium block site.
2. The oriented α-helices contribute importantly to ion stabilization at the interior sites of the filter, again with implications for the stabilization of divalent ions.

Preliminary work incorporating flexibility indicates that movement of the α-helical termini substantially affects co-operativity, and suggests that electrostatically induced reorientation of moieties quite distant from the solvated ion(s) may significantly influence stabilization of the filter's ionic contents.

We presented a new approach allowing reconciliation of the requirement of self-adjustment of the membrane deformation profile (relaxed boundary conditions) with (1) the notion that membrane properties must be modified at short distances from the inser-

tion, and (2) the comparatively high experimental values of the elastic energy of insertion. This model suggests certain local stiffening of the membrane elastic constants. This should affect lipid fluctuations in the vicinity of insertions and may be experimentally studied using neutron scattering, x-ray scattering, and spin labeling techniques, and computationally, using molecular dynamics simulation.

In our discussion of deformation phenomena, some important features were not considered (due to space limitations). One of them, which has received much attention, is the influence of the monolayer equilibrium curvature on the membrane deformation [91,133]. These features should be addressed in further development of the nonuniform model.

The elastic membrane model, formulated in terms of elastic moduli and $u(r)$, provides a significantly reduced description of insertion phenomena. More detailed analysis should account for the orientation and displacement of the lipid molecules as well as some of their internal degrees of freedom. A step in this direction has been made, for instance, in Ref. 95. At short-length scales and near nonuniformities, lipid molecules cannot attain the "normal" orientations typical of their mean behavior on a macroscopic scale, which must inevitably affect their elastic properties. More detailed statistical mechanical analysis and simulational studies might provide useful insight into such behavior.

Nonmonotonic behavior of membrane-mediated interactions and significant many-body effects could be responsible for the complex phase behavior of the peptides incorporated in the membranes, and its dependence on the membrane lipid composition. Interestingly, a similar variation of the interaction potential for two insertions (of radii $r_0 = 9$ Å) as a function of lipid composition has been found recently in a simulational study [132]. We are planning to study these transitions in the composition–protein concentration phase plane. Another interesting issue is the possibility that peptide clustering can affect the lifetime of ion channels, a study which is already under way.

ACKNOWLEDGMENTS

We greatly appreciate valuable and stimulating discussions with Dr. Yury Neustadt (Samara State University, Russia) about various problems in the theory of elastic plates and shells. This work was supported by the National Center for Supercomputing Applications and by the National Institutes of Health, Grant no. GM-28643.

REFERENCES

1. B Hille. Ionic Channels of Excitable Membranes. Sunderland, MA: Sinauer Associates, 1992.
2. P Agre, GM Preston, BL Smith, JS Jung, S Raina, C Moon, WB Guggino, S Nielsen. Am J Physiol 265:F463–F476, 1993.
3. C Maurel, J Reizer, JI Schroeder, MJ Chrispeels, MH Saier. J Biol Chem 269:11869–11872, 1994.
4. P Läuger. Electrogenic Ion Pumps. Sunderland, MA: Sinauer Associates, 1991.
5. DW Doyle, JM Cabral, RA Pfuetzner, A Kuo, J Gulbis, SL Cohen, BT Chait, R MacKinnon. Science 280:69–77, 1998.
6. A Solomon. J Gen Physiol 51:335s–364s, 1968.
7. DG Levitt. Biophys J 13:186–206, 1973.
8. DP Tieleman, PC Biggin, GR Smith, MSP Sansom. Q Rev Biophys 34:473–561, 2001.

9. VL Dorman, MB Partenskii, PC Jordan. Biophys J 70:121–134, 1996.
10. VL Dorman, S Garofoli, PC Jordan. In: DJ Chadwick, G Cardew, eds. Gramicidin and Related Ion-Channel Forming Peptides. Chichester, UK: John Wiley, 1999, pp 153–169.
11. S Garofoli, G Miloshevsky, VL Dorman, PC Jordan. In: DJ Chadwick, J Goode, eds. Ion Channels—from Atomic Resolution to Functional Genomics. Chichester, UK: John Wiley, 2002, pp 109–122.
12. S Koneshan, JC Rasaiah, RM Lynden-Bell, SH Lee. Phys Chem B 102:4193–4204, 1998.
13. DA Dougherty. Science 271:163–168, 1996.
14. AS Arseniev, AL Lomize, IL Barsukov, VF Bystrov. Biolog Membr (USSR) 3:1077–1104, 1986.
15. TA Cross. Methods Enzymol 289:672–696, 1997.
16. R Dutzler, EB Campbell, M Cadene, BT Chart, R MacKinnon. Nature 415:287–294, 2002.
17. G Chang, RH Spencer, ATL At, MT Barclay, DC Rees. Science 282:2220–2226, 1998.
18. K Murata, K Mitsuoka, T Hirai, T Walz, P Agre, JB Heymann, A Engel, Y Fujiyoshi Nature. 407:599–605, 2000.
19. D Fu, A Libson, LJW Miercke, C Weitzman, P Nollert, J Krucinski, RM Stroud. Science 290:481–486, 2000.
20. SH Heinemann, H Terlau, W Stühmer, K Imoto, S Numa. Nature 356:441–443, 1992.
21. J Yang, PT Ellinor, WA Sather, JF Zhang, RW Tsien. Nature 366:158–161, 1993.
22. A Myazawa, Y Fujiyoshi, M Stowell, N Unwin. J Mol Biol 288:765–786, 1999.
23. K Imoto, C Busch, B Sakmann, M Mishina, T Konno, J Nakai, H Bojo, Y Mori, K Fukuda, S Numa. Nature 335:645–648, 1988.
24. DJ Adams, TM Dwyer, B Hille. J Gen Physiol 75:493–510, 1980.
25. C Miller, Phil Trans Roy Soc London B 299:401–411, 1982.
26. B Roux. Biophys J 71:3177–3185, 1996.
27. J Neyton, C Miller. J Gen Physiol 92:569–586, 1988.
28. TW Allen, A Bliznyuk, AP Rendell, S Kuyucak, S-H Chung. J Chem Phys 112:8191–8204, 2000.
29. D Meuser, H Splitt, R Wagner, H Schrempf. FEBS Lett 462:447–452, 1999.
30. E Jakobsson, S-W Chiu. Biophys J 52:33–45, 1987.
31. SW Chiu, E Jakobsson, S Subramaniam, JA McCammon. Biophys J 70:121–134, 1991.
32. B Roux, M Karplus. Annu Rev Biophys Biomol Struct 23:731–761, 1994.
33. R Pomés, B Roux. Biophys J 71:19–39, 1996.
34. TB Woolf, B Roux. Biophys J 68:876–892, 1997.
35. B Jayaram, DL Beveridge. Annu Rev Biophys Biomol Struct 25:367–394, 1996.
36. WL van Gunsteren, FJ Luque, D Timms, AE Torda. Annu Rev Biophys Biomol Struct 23:847–863, 1994.
37. S Tanizaki, PC Jordan, unpublished results, 2000.
38. GC Groeneboom, E Mas, R Bukowski, K Szalewicz, PES Wormer, A van der Avoird. Phys Rev Lett 84:4072–4075, 2000.
39. IH Shrivastava, MSP Sansom. Biophys J 78:557–570, 2000.
40. J Åqvist, V Luzhkov. Nature 404:881–884, 2000.
41. S Berneche, B Roux. Biophys J 78:2900–2917, 2000.
42. L Guidoni, V Torre, P Carloni. FEBS Lett 477:37–42, 2000.
43. TW Allen, S Kuyucak, S-H Chung. Biophys J 77:2502–2516, 1999.
44. PC Biggin, GR Smith, I Shrivastava, S Choe, MSP Sansom. Biochim Biophys Acta 1510:1–9, 2001.
45. B Corry, TW Allen, S Kuyucak, S-H Chung. Biochim Biophys Acta 1509:1–6, 2000.
46. D Boda, DD, Busath, D Henderson, S Sokolowski. J Phys Chem B 104:8903–8910, 2000.
47. W Nonner, L Catacuzzeno, B Eisenberg. Biophys J 79:1976–1992, 2000.
48. W Nonner, D Gillespie, D Henderson, B Eisenberg. J Phys Chem B 105:6427–6436, 2001.
49. B Roux, R MacKinnon. Science 285:100–102, 1999.
50. SH Chung, TW Allen, M Hoyles, S Kuyucak. Biophys J 77:2517–2533, 1999.

51. M Partenskii, M Cai, P Jordan. Chem Phys 153:125–131, 1991.
52. M Partenskii, M Cai, P Jordan. Electrochim Acta 36:1753–1756, 1991.
53. MB Partenskii, PC Jordan. Quart Rev Biophys 24:477–510, 1992.
54. MB Partenskii, VL Dorman, PC Jordan. Biophys J 67:1429–1438, 1994.
55. BR Brooks, RE Bruccoleri, BD Olafson, DJ States, S Swaminathan, M Karplus. J Comput Chem 4:187–217, 1983.
56. SJ Weiner, PA Kollman, DA Case, UC Singh, C Ghio, G Alagona, S Profeta Jr, P Weiner. J Am Chem Soc 106:765–784, 1984.
57. HJC Berendsen, JPM Postma, WF van Gunsteren, J Hermans. In: B. Pullman, eds. Intermolecular Forces. Dordrecht: Reidel, 1981, pp 331–342.
58. JB Hasted. In: F Franks, ed. Water, a Comprehensive Treatise. vol. 1. New York: Plenum Press, 1973, pp 405–458.
59. DR Lide, ed. Handbook of Chemistry and Physics. 78th ed. Boca Raton, FL: CRC Press, 1998.
60. VL Dorman, PC Jordan. J. Chem. Phys. (submitted).
61. L Pauling. The Nature of the Chemical Bond. 3rd ed. Ithaca, NY: Cornell University Press, 1960.
62. E Grunwald. Thermodynamics of Molecular Species. New York: Wiley-Interscience, 1997.
63. H Reiss, A Heller. J Phys Chem 89:4207–4213, 1985.
64. MD Tissandier, KA Cowan, WY Feng, E Gundlach, MH Cohen, AD Earhart, JV Coe, TR Tuttle. J Phys Chem A 102:7787–7794, 1998.
65. DL Beveridge, GW Schnuelle. J Phys Chem 79:2562–2566, 1975.
66. PC Jordan. Ionic energetics in narrow channels. Proceedings of the IMA Workshop on Membrane Transport and Renal Physiology. New York: Springer-Verlag, 2002.
67. JA Odutola, TR Dyke. J Chem Phys 72:5062–5070, 1980.
68. R Guidelli. J Chem Phys 92:6152–6160, 1990.
69. Y Jiang, R MacKinnon. J Gen Physiol 115:269–272, 2000.
70. PC Jordan. Mol Phys 25:961–973, 1973.
71. PC Jordan. Chemical Kinetics and Transport. New York: Plenum Press, 1979.
72. G Miloshevsky, PC Jordan, 2001.
73. OS Andersen, RE Koeppe II. Physiol Rev 72:S89–S158, 1992.
74. P Devaux, M Seigneuret. Biochim Biophys Acta 822:63–125, 1983.
75. A Bienvenue, J Marie. Curr Top Membr 40:319–354, 1994.
76. C Nielsen, M Goulian, OS Andersen. Biophys J 74:1966–1983, 1998.
77. SM Bezrukov, RP Rand, I Vodyanoy, VA Parsegian, Faraday Disc 111:173, 1998.
78. S Keller, S Bezrukov, S Gruner, W Tate, I Vodyanoy, VA Parsegian. Biophys J 65:23–27, 1993.
79. K Åkerfeldt, J Lear, Z Wasserman, L Chung, W Degrado. 26:191–197, 1993.
80. K Jakes, P Kienker, A Finkelstein. Q Rev Biophys 32:189–205, 1999.
81. K Oh, L Senzel, R Collier, A Finkelstein. Proc Nat Acad Sci USA 96:8467–8470, 1999.
82. B Litman, D Mitchell. Lipids 31:S193, 1996.
83. C Huang, S Feng, DW Hilgemann. Nature 391:803–806, 1998.
84. Z He, S Feng, Q Tong, D Hilgemann, K Philipson. Am J Physiol 278:C661–C666, 2000.
85. L Landau, E Lifshitz. Theory of Elasticity. Oxford: Butterworth-Heinemann, 1970.
86. S Timoshenko, S Woinowsky-Krieger. Theory of Plates and Shells. New York: McGraw-Hill, 1959.
87. H Huang. Biophys J 50:1061–1070, 1986.
88. P Helfrich, E Jakobsson. Biophys J 57:1075–1084, 1990.
89. T Harroun, W Heller, T Weiss, L Yang, H Huang. Biophys J 76:3176–3185, 1999.
90. H Aranda-Espinoza, A Berman, N Dan, P Pincus, S Safran. Biophys J 71:648–656, 1996.
91. C Nielsen, OS Andersen. Biophys J 79:2583–2604, 2000.
92. H Hertz. Wiedemann's Ann Phys Chem 22:449–461, 1884.
93. F Schleicher. Kreisplatten auf elasticher Unterlage. Berlin: Springer, 1926.

94. N Dan, A Berman, P Pincus, S Safran. J Phys II (France) 4:1713–1725, 1994.
95. A Ring. Biochim Biophys Acta 1278:147–159, 1996.
96. J Owicki, M Springgate, H McConnell. Proc Natl Acad Sci USA 75:1616–1619, 1978.
97. JC Owicki, HM McConnell. Proc Natl Acad Sci USA 76:4750–4754, 1979.
98. P-G de Gennes, J Prost. The Physics of Liquid Crystals. Oxford: Clarendon Press, 1995.
99. D Bensimon, F David, S Leibler, A Pumir. J Phys France 51:659–695, 1990.
100. M Bloom, E Evans, O Mouritsen. Q Rev Biophys 24:293–397, 1991.
101. D Sornette, N Ostrowsky. In: W Gelbart, A Ben-Shaul, D Roux, eds. Micelles, Membranes, Microemulsions, and Monolayers. New York: Springer-Verlag, 1994, pp 251–302.
102. D Marsh. Biochim Biophys Acta 1286:183–223, 1996.
103. F Jahning. Biophys J 71:1348–1349, 1996.
104. SE Feller, R Pastor. Biophys J 71:1350–1355, 1996.
105. R Goetz, R Lipowsky. J Chem Phys 108:7397–7409, 1998.
106. H Tien, A Ottova-Leitmannova. Membrane Biophysics as viewed from Experiemental Bilayer Lipid Membraness. Amsterdam, New York: Elsevier, 2000.
107. MB Partenskii, PC Jordan. Biophys J 78:325A, 2000.
108. M Goulian, O Mesquita, D Fygenson, C Nielsen, O Andersen, A Libchaber. Biophys J 74:328–337, 1998.
109. MB Partenskii, PC Jordan. Mol Phys 98:193–200, 2000.
110. MB Partenskii, PC Jordan. Biophys J 80:544A, 2001.
111. JA Lundbæk, O Andersen. Biophys J 76:889–895, 1999.
112. J Elliot, D Needham, J Dilger, D Haydon. Biochim Biophys Acta 735:95–103, 1983.
113. H Kolb, E Bamberg. Biochim Biophys Acta 464:127–141, 1977.
114. J Boon, S Yip. Molecular Hydrodynamics. New York: Dover Publications, 1980.
115. M Partenskii, V Dorman, P Jordan. In: R Lieberman, T Vo-Dinh. Progress in Biomedical Optics. Proceedings of Biomedical Sensing and Image Technologies. vol. 3253. San-Jose, CA: SPIE, 1998, pp 266–278.
116. M Partenskii, V Dorman, P Jordan. J Chem Phys 109:10361–10371, 1998.
117. M Partenskii, P Jordan. In: AG Volkov, ed. Liquid Interfaces in Chemical, Biological, and Pharmaceutical Applications, vol. 95 of Surfactant Science Series. New York: Marcel Dekker 2001, pp 51–82.
118. K Mecke, S Dietrich. Phys Rev E 59:6766–6784, 1999.
119. C Fradin, A Braslau, D Luzet, D Smilgies, M Alba, N Boudet, K Mecke, J Daillant. Nature 403:871–874, 2000.
120. S Chen, CY Liao, H Huang, T Weiss, M Bellisent-Funel, F Sette. Phys Rev Lett 86:740–743, 2001.
121. S Wolfram. The Mathematica Book. 4th ed. New York: Cambridge University Press, 1999.
122. W Rawicz, K Olbrich, T McIntosh, D Needham, E Evans. Biophys J 79:328–339, 2000.
123. T Woolf, B Roux. Proteins Struct Funct Genet 24:92–114, 1996.
124. H Petrache, J Killian, RI Koeppe, T Woolf. Biophys J 78:342A, 2000.
125. D Fattal, A Ben-Shaul. Biophys J 65:1795–1809, 1993.
126. P Kralchevsky, V Paunov, N Denkov, K Nagayama. J Chem Soc, Faraday Trans 5:3415–3432, 1995.
127. M Goulian, R Bruinsma, P Pincus. Europhys Lett 22:145–150, 1993.
128. J Kim, KS Neu, G Oster. Biophys J 75:2274–2291, 1998.
129. N Dan, P Pincus, S Safran. Langmuir 9:2768–2774, 1993.
130. K Morton, D Mayers. Numerical Solution of Partial Differential Equations. Cambridge, UK: Cambridge University Press, 1994.
131. G Miloshevsky, M Partenskii, P Jordan. (2002), in preparation.
132. P Lague, M Zuckermann, B Roux. Biophys J 81:276–284, 2001.
133. N Dan, S Safran. Biophys J 75:1410–1414, 1998.